

1 **Spacecraft plume interactions with the**  
2 **magnetosphere plasma environment in geostationary**  
3 **Earth orbit**

K. A. Stephani<sup>1</sup> and I. D. Boyd<sup>2</sup>

---

<sup>1</sup>Department of Mechanical Science and  
Engineering, University of Illinois  
Urbana-Champaign, Urbana, Illinois, USA.

<sup>2</sup>Department of Aerospace Engineering,  
University of Michigan, Ann Arbor,  
Michigan, USA.

This is the author manuscript accepted for publication and has undergone full peer review but has not been through the copyediting, typesetting, pagination and proofreading process, which may lead to differences between this version and the Version of Record. Please cite this article as doi:

10.1029/2015JA021158

February 3, 2016, 5:18am

D R A F T

4 **Abstract.** Particle-based kinetic simulations of steady and unsteady hy-  
5 drazine chemical rocket plumes are presented in a study of plume interac-  
6 tions with the ambient magnetosphere in geostationary Earth orbit (GEO).  
7 The hydrazine chemical rocket plume expands into a near-vacuum plasma  
8 environment, requiring the use of a combined direct simulation Monte Carlo/Particle-  
9 in-Cell methodology for the rarefied plasma conditions. Detailed total and  
10 differential cross sections are employed to characterize the charge exchange  
11 reactions between the neutral hydrazine plume mixture and the ambient hy-  
12 drogen ions, and ion production is also modeled for photoionization processes.  
13 These ionization processes lead to an increase in local plasma density sur-  
14 rounding the spacecraft owing to a partial ionization of the relatively high-  
15 density hydrazine plume. Results from the steady plume simulations indi-  
16 cate that the formation of the hydrazine ion plume are driven by several com-  
17 peting mechanisms, including (i) local depletion and (ii) replenishing of am-  
18 bient  $H^+$  ions by charge exchange and thermal motion of 1 keV  $H^+$  from the  
19 ambient reservoir, respectively, and (iii) photoionization processes. The self-  
20 consistent electrostatic field forces and the geostationary magnetic field have  
21 only a small influence on the dynamics of the ion plume. The unsteady plume  
22 simulations show a variation in neutral and ion plume dissipation times con-  
23 sistent with the variation in relative diffusion rates of the chemical species,  
24 with full  $H_2$  dissipation (below the ambient number density levels) approx-  
25 imately 33 seconds after a two-second thruster burn.

## 1. Introduction

26   Spacecraft in orbit use thruster burns for orbital maneuvers including changes in orbital  
27 inclination and delta-V maneuvers. The plumes that form as a result of these burns  
28 are very high in density relative to the near-vacuum ambient environment, presenting  
29 significant challenges concerning plume impingement on spacecraft surfaces. Direct plume  
30 impingement can generate unwanted torques on the spacecraft, as well as localized heating  
31 and contamination of sensitive surfaces. Predictive capabilities to assess and mitigate  
32 plume impingement on critical spacecraft surfaces rely on models that capture the non-  
33 equilibrium nature of the plume expansion, as well as the interaction of the plume with the  
34 ambient plasma environment. Neutral post-combustion constituents in chemical rocket  
35 plumes are subject to charge-exchange interactions with the ambient space plasma, which  
36 lead to the formation of a high-density ion plume. A fundamental understanding of plume  
37 interactions with the ambient plasma is thus imperative for the characterization of plume  
38 dynamics, especially concerning plume impingement issues.

39   A number of experimental (laboratory and *in situ*) and computational studies have  
40 been conducted to assess the effects of plume interaction and impingement on spacecraft  
41 surfaces (*Burke et al.* [1995]; *McMahon et al.* [1983]; *Karabadzhak et al.* [1997]; *Drakes and*  
42 *Swann* [1999]; *Kaplan and Bernhardt* [2010]; *Bernhardt et al.* [2012]). *Burke et al.* in par-  
43 ticular presented measurements of positive, single-charge ion energy distributions detected  
44 during thruster burns of the Tethered Satellite System (TSS 1) mission by the Shuttle Po-  
45 tential and Return Electron Experiment (SPREE). These measurements reported energy  
46 and angular distributions of pickup ions (ions formed through charge-exchange reactions

47 between thruster neutral particles and ambient ions) impacting the sensor. In comparison  
48 of these results to predicted ion trajectories from a collisionless two-dimensional simula-  
49 tion model, it was concluded that strong scattering must occur near the highly collisional  
50 thruster exit to account for the main features of the detected ion energy spectra. These  
51 studies focused primarily on the influence of the magnetic field on pickup ion trajectories,  
52 and were limited to relatively short-range detection distances.

53 Additional computational models, including direct simulation Monte Carlo (DSMC),  
54 and ray-tracing and particle-tracing methods, have been developed to aid in the pre-  
55 diction of plume interaction with the ambient environment and with spacecraft surfaces  
56 (*Alexeenko et al.* [2004]; *Ngalande et al.* [2006]; *Yim et al.* [2014]). These models have been  
57 used to investigate plume contamination characteristics (*Alexeenko et al.* [2004]), surface  
58 heating due to plume impingement (*Yim et al.* [2014]) and effects of surface roughness on  
59 near-field plume development (*Ngalande et al.* [2006]). Although these models address the  
60 collisional aspect of the plume, the studies have been largely focused on spacecraft plume  
61 interactions over relatively small distances, and neglect environmental considerations from  
62 charge-exchange reactions or electrostatic and magnetic field effects. Incorporating these  
63 effects is critical for capturing the development of the spacecraft plume in the plasma  
64 environment, particularly over large distances. Recent efforts (*Stephani and Boyd* [2014];  
65 *Stephani et al.* [2014]) investigating spacecraft plumes in low Earth orbit (LEO) have  
66 demonstrated that interaction of the spacecraft neutral plume with the ambient plasma  
67 forms a relatively high-density spacecraft ion plume. The propagation of this ion plume  
68 is determined primarily by the interaction with the magnetic field, but the development



69 of the neutral spacecraft plume is also affected (albeit indirectly) by the magnetic field  
70 interaction owing to secondary charge-exchange reactions.

71 The present study aims to examine the interaction between spacecraft hydrazine  
72 thruster plumes and the ambient magnetosphere in geostationary Earth orbit (GEO)  
73 conditions. While previous efforts have developed a combined direct simulation Monte  
74 Carlo/Particle in Cell (DSMC/PIC) methodology to examine plumes in LEO (*Stephani*  
75 *and Boyd* [2014]; *Stephani et al.* [2014]), this study focuses on the additional physical  
76 model considerations involving non-equilibrium plasma mixtures. The rarefied nature  
77 of the magnetosphere, as well as the presence of the surrounding plasma environment,  
78 requires the use of a combined DSMC/PIC methodology, which is detailed next. The am-  
79 bient conditions in the magnetosphere present an environment in which photoionization  
80 processes become comparable to charge transfer processes, contrary to the LEO envi-  
81 ronment. Results are presented for both steady and unsteady spacecraft thruster burns,  
82 in which the neutral rocket plume is modeled as a mixture of three primary propellant  
83 species. The influence of both charge transfer and photoionization processes on the de-  
84 velopment of the neutral and ion plumes are also investigated.

## 2. Modeling of Plume/Magnetosphere Interactions

### 2.1. DSMC/PIC Framework

85 The charge exchange collisions between ambient ions and rocket plume combustion  
86 species occur under very low density conditions. The most appropriate numerical method  
87 for simulation of these phenomena is the direct simulation Monte Carlo (DSMC) method  
88 (*Bird* [1994]). The plasma formed in this process is subject to self-consistent electro-  
89 static fields, which is most appropriately modeled using the Particle in Cell (PIC) method

90 (*Birdsall and Langdon [2004]*). The combination of rarefied collisional and plasma  
91 phenomena relevant to the physical system of interest is therefore analyzed using MPIC  
92 (*Cai [2005]*), which uses the DSMC and PIC methods simultaneously to model the flow  
93 field.

## 2.2. MEX/CEX Collision Dynamics and Photoionization

94 The ambient magnetosphere model used in this study is comprised of  $H^+$ , the primary  
95 ion species found at GEO. The spacecraft thruster ejects a high-density plume of neutral  
96 particles which expands into the surrounding ambient flow. Interaction of the chemical  
97 rocket plume mixture with the ambient  $H^+$  leads to the formation of an ion plume mixture  
98 through charge exchange (CEX) reactions. The chemical system under consideration  
99 is thus comprised of seven chemical species: the ambient  $H^+$  ions, and the hydrazine  
100 combustion products,  $H_2$ ,  $N_2$  and  $NH_3$  and their corresponding ions,  $H_2^+$ ,  $N_2^+$  and  $NH_3^+$ .

101 The ambient  $H^+$  ions are allowed to participate in both momentum exchange (MEX) and  
102 CEX interactions with the plume constituents, but the post-collision properties of  $H^+$  are  
103 updated in order to simulate the local depleting/replenishing of  $H^+$  in the vicinity of the  
104 spacecraft plume. The ambient  $H^+$  ions are depleted upon charge exchange with spacecraft  
105 neutral particles, forming neutral H atoms, but the surrounding ambient provides an  
106 infinite reservoir of  $H^+$  ions at 1 keV to replenish the local population. This replenishing  
107 process is modeled as a finite-rate reactivation of ambient H neutrals to ions. The rate of  
108 reactivation is based on the time-of-flight for a 1 keV  $H^+$  ion to reach the position of the  
109 H neutral from an infinite reservoir at  $x = -20$  km. As will be seen in the steady-state  
110 simulation results, the infinite reservoir is taken at the  $x$ -location where the steady-state  
111 neutral plume density falls off below the ambient density.

112 Photoionization processes involving the ionization of spacecraft neutrals are also in-  
 113 cluded in this model. The photoionization collision frequency is based on integration of  
 114 the product of the photoionization cross section with Planck's spectral black-body emis-  
 115 sive power with respect to wavelength. The resulting collision frequencies employed in  
 116 these calculations are  $O(1 \times 10^{-6})$  collisions per second.

117 All of the chemical species comprising the spacecraft plume mixture participate in  
 118 MEX/CEX interactions, and binary collisions and post-collision scattering are computed  
 119 based on detailed total and differential cross sections. The rotational, vibrational and  
 120 electronic internal structure of plume constituents is currently neglected in this work.

121 The collision details involving plasma mixtures requires a careful treatment for collisions  
 122 between neutral and charged particles, particularly in cases where the collision partners  
 123 are not like species. Within the DSMC method, collision dynamics are imposed in the  
 124 center-of-mass frame of reference of the colliding particles. Collisions involving two neu-  
 125 tral particles are processed using the Variable Hard Sphere (VHS) model, in which the  
 126 probability of a collision is computed according to:

$$P = \frac{\sigma g}{(\sigma g)_{max}}, \quad (1)$$

127 where  $\sigma$  is the total cross section and  $g$  is the relative collision speed, and a candidate pair  
 128 is selected for collision if  $P > \mathcal{R}_u$ , where  $\mathcal{R}_u$  is a uniformly distributed random number.  
 129 Heavy particle interactions are treated according to standard DSMC collision dynamics,  
 130 with the possibility of a charge transfer for neutral/ion collision pairs. The total number  
 131 of candidate collision partners within a cell is determined using Bird's No-Time-Counter  
 132 (NTC) (*Bird* [1994]) method. The probability of a collision event is then determined for

133 these candidate pairs based on the total collision cross section. MEX collisions for neutral  
 134 particle interactions are modeled using variable hard sphere (***Bird* [1994]**) (VHS) total  
 135 cross sections and isotropic scattering. The corresponding VHS parameters including the  
 136 reference diameter  $d_{ref}$ , reference temperature  $T_{ref}$ , and temperature exponent  $\omega$  for the  
 137 gas mixture constituents are provided in Table 1.

138 Post-collision velocities involving neutral collision pairs are assumed to follow isotropic  
 139 scattering in the center-of-mass frame of reference. Collisions involving neutral/ion pairs,  
 140 however, scatter anisotropically, with a strong forward-scattering tendency. Total and  
 141 differential cross section data for this system are obtained from the literature (***Kusakabe***  
 142 ***et al.* [2000]; *Cabrera et al.* [2002]; *Coplan and Ogilvie* [1970]) for both direct  
 143 and charge transfer collisions based on guided ion beam experimental results and the  
 144 electron nuclear dynamics formalism. While the total cross section is invariant under  
 145 transformation of reference frame, the differential cross section must be converted from  
 146 the laboratory (LAB) reference frame to the center-of-mass (CM) reference frame for use  
 147 within the DSMC/PIC framework. The differential cross section (DCS) transformation is  
 148 established through the relationship between the LAB and CM total cross-sectional area:**

$$\frac{d\sigma(\theta_{CM})}{d\Omega_{CM}} d\Omega_{CM} = \frac{d\sigma(\theta_{LAB})}{d\Omega_{LAB}} d\Omega_{LAB} \quad (2)$$

149 where:

$$d\Omega_{CM} = 2\pi \sin(\theta_{CM}) d\theta_{CM}, \quad (3)$$

$$d\Omega_{LAB} = 2\pi \sin(\theta_{LAB}) d\theta_{LAB}. \quad (4)$$

150 For a LAB  $\rightarrow$  CM transformation, Eq 2 is written as:

$$\frac{d\sigma(\theta_{CM})}{d\Omega_{CM}} = \frac{d\sigma(\theta_{LAB})}{d\Omega_{LAB}} \frac{d\Omega_{LAB}}{d\Omega_{CM}} = \frac{d\sigma(\theta_{LAB})}{d\Omega_{LAB}} \frac{\sin(\theta_{LAB})d\theta_{LAB}}{\sin(\theta_{CM})d\theta_{CM}} \quad (5)$$

151  
152  
153 The transformation is established by obtaining an analytical expression (if possible) for  
154 the term on the far right hand side of Eq 5. The relationship between  $\theta_{LAB}$  and  $\theta_{CM}$  may  
155 be determined by considering the schematic of scattering of two particles A and B in the  
156 center-of-mass (CM) frame of reference shown in Figure 1. If the particle B is considered  
157 to be at rest in the laboratory frame of reference, then the point B lies on the dashed circle  
158 with a radius  $p_0 = \mu v$ , where  $\mu = m_1 m_2 / (m_1 + m_2)$  is the reduced mass and  $v = v_1 - v_2$   
159 is the relative velocity prior to collision. In the case when  $m_1 = m_2$ , both A and B lie on  
160 the dashed circle, and it is straight-forward to show that the relationship between  $\theta_{LAB}$   
161 and  $\theta_{CM}$  is:

$$\theta_{CM} = 2\theta_{LAB} \quad (6)$$

162 resulting in the differential cross section transformation for direct or (resonant) charge  
163 transfer collisions:

$$\frac{d\sigma(\theta_{LAB})}{d\Omega_{LAB}} = 4 \cos \theta_{LAB} \frac{d\sigma(\theta_{CM})}{d\Omega_{CM}} \quad (7)$$

164

165

166 In the gas mixture, it is necessary to account for cases where  $m_1 \neq m_2$ . To simplify the  
 167 analysis, we assume that  $v_1 \gg v_2$  such that the second particle is at rest, and point B thus  
 168 lies on the dashed circle as in Figure 1. This is a reasonable assumption at GEO, since  
 169 the  $H^+$  are approximately 1 keV, and the hydrazine chemical species are characterized by  
 170 energies of less than 1 eV. Following this approach then, we have that  $m_1$  corresponds  
 171 to  $m_{H^+}$ , and  $m_1 < m_2$  regardless of the collision partner for all chemical species in the  
 172 hydrazine mixture, as shown in Figure 1.

173  
 174 Invoking the sum of angles and law of sines, we can establish the relationship between  
 175 the scattering angle of particle 1 ( $H^+$  in this case) in the LAB frame ( $\theta_{LAB}$ ) and the CM  
 176 frame ( $\theta_{CM}$ ), and finally the expressions for  $\sin \theta_{LAB}$  and  $d\theta_{LAB}$  which are required for  
 177 the transformation:

$$\theta_{CM} = \theta_{LAB} + \sin^{-1} \left( \frac{m_1}{m_2} \sin \theta_{LAB} \right) \quad (8)$$

$$d\theta_{CM} = 1 + \frac{m_1/m_2 \cos \theta_{LAB}}{\sqrt{1 - (m_1/m_2)^2 \sin^2 \theta_{LAB}}} \quad (9)$$

$$\sin \theta_{CM} = \sin \left[ \theta_{LAB} + \sin^{-1} \left( \frac{m_1}{m_2} \sin \theta_{LAB} \right) \right] \quad (10)$$

178 The transformation can be made by expressing the right hand side of Equation 5 in terms  
 179 of  $\theta_{CM}$  and then plotting the CM DCS as a function of  $\theta_{CM}$ . However, Equations 8 - 10  
 180 can only be solved approximately using an iterative solution approach, so an immediate  
 181 analytical form is not possible. If instead the right hand side is left in terms of  $\theta_{LAB}$ , the  
 182 final LAB  $\rightarrow$  CM transformation is expressed as:

$$\frac{d\sigma(\theta_{CM})}{d\Omega_{CM}} = \frac{\sin \theta_{LAB}}{\sin \left[ \theta_{LAB} + \sin^{-1} \left( \frac{m_1}{m_2} \sin \theta_{LAB} \right) \right]} \left( 1 + \frac{m_1/m_2 \cos \theta_{LAB}}{\sqrt{1-(m_1/m_2)^2 \sin^2 \theta_{LAB}}} \right) \frac{d\sigma(\theta_{LAB})}{d\Omega_{LAB}} \quad (11)$$

183 The right hand side is evaluated with a value for the LAB DCS and the corresponding  
 184 angle  $\theta_{LAB}$  (from experimental data), and finally the transformed value for the CM DCS is  
 185 obtained. These values are plotted against  $\theta_{CM}$ , which is determined for each value of  $\theta_{LAB}$   
 186 from Equation 8. This transformation is applied to the differential cross sections describing  
 187 the post-collision scattering of  $H_2 - H^+$ ,  $N_2 - H^+$  and  $NH_3 - H^+$  collision partners in the  
 188 center-of-mass frame of reference, and the resulting cross sections are plotted in Figure  
 189 2(a). The LAB→CM transformation is most prominent for cases in which the collision  
 190 partners are of equal mass ( $m_1 = m_2$ ), and the differential cross section in the CM frame  
 191 of reference approaches the LAB frame value when  $m_1 \ll m_2$ . Total direct (non-transfer)  
 192 and charge transfer cross sections employed in this model are reported in the literature for  
 193 the mixture constituents (*Kusakabe et al.* [2000]; *Cabrera et al.* [2002]; *Coplan*  
 194 *and Ogilvie* [1970]), and the charge transfer cross sections are shown in Figure 2(b).

### 2.3. Magnetic Field Model

195 In addition to CEX and photoionization interactions, charged particles in GEO are sub-  
 196 ject to interaction with Earth's magnetic field. Previous studies in the LEO environment  
 197 have demonstrated the important role that the magnetic field plays in the propagation of  
 198 the ion plume. The magnetic field strength at GEO, however, is considerably weaker, and  
 199 the spacecraft on average is stationary with respect to the field lines. The magnetic field  
 200 model employed in this work is adopted from previous studies at low Earth orbit, and  
 201 has been extended for plasma mixtures. The gyroscopic motion of the charged particles is

202 dependent upon the ion mass through the Larmor radius,  $r_L$ , and the gyration frequency,  
 203  $\omega_L$ , which are determined according to:

$$r_L = \frac{V_{x0}^{ion}}{\omega_L}, \quad (12)$$

$$\omega_L = \frac{q^{ion} B}{m^{ion}}. \quad (13)$$

204 In Eq. 12,  $V_{x0}^{ion}$  is the initial x-velocity of the  $\text{H}_2^+/\text{N}_2^+/\text{NH}_3^+$  species entering the gyro-orbit,  
 205 which is equivalent to the post-collision x-velocity after a charge exchange reaction. In  
 206 Eq. 13,  $q^{ion}$  is the fundamental charge,  $B$  is the magnetic field strength, and  $m^{ion}$  is the  
 207 molecular mass of the  $\text{H}_2^+/\text{N}_2^+/\text{NH}_3^+$  species.

208 The magnetic field lines in these simulations are assumed to be perpendicular to the  
 209 thrust vector (aligned with the  $x$ -direction). A full outline of the magnetic field model is  
 210 presented in *Stephani and Boyd* [2014]. The significance of the magnetic field interaction  
 211 with the charged hydrazine plume species,  $\text{H}_2^+$ ,  $\text{N}_2^+$  and  $\text{NH}_3^+$ , was established by investi-  
 212 gating magnetic field strengths of  $B=1.1 \times 10^{-7}$  T (at GEO) and a limiting case of  $B \rightarrow 0$ .  
 213 The magnetic field is found to have only a minor influence on the ion plume development,  
 214 and a negligible influence on the neutral plume development for the conditions presented  
 215 here.

## 2.4. Plume Configurations

216 The plume interactions investigated in this study address both steady and unsteady  
 217 firings of a hydrazine spacecraft thruster into the ambient magnetosphere free stream in  
 218 GEO. The spacecraft thruster is located at the origin  $(x, z) = 0$ , and generates thrust  
 219 in the  $-x$ -direction. The plume flow is simulated on an axisymmetric computational



220 domain with a radius of 35 km, which is shown in Figure 3. The plume flow at the  
221 thruster exit is in the  $+x$ -direction, as indicated by the red arrow. A mass flow rate of  
222  $\dot{m} = 5.0 \times 10^{-4}$  kg/s is specified through an inflow boundary condition at the nozzle exit  
223 plane (not visible in Figure 3). The exit plane flow is modeled as a neutral propellant  
224 mixture of molecular hydrogen, nitrogen and ammonia, with the properties shown in  
225 Table 2. The computational frame of reference is held fixed with respect to the spacecraft  
226 thruster, so the ambient  $H^+$  ions follow a thermal distribution in this frame of reference.  
227 Recalling discussion of the magnetic field model, the geostationary magnetic field lines  
228 are assumed to be aligned vertically along the  $+z$ -axis in the computational domain, and  
229 are assumed to be stationary relative to the spacecraft thruster.

230 Typical values of the spacecraft propellant ion gyroscopic radii are summarized in Table  
231 3, based on a nominal magnetic field strength of  $B=1.1 \times 10^{-7}$  T including diurnal variation  
232 (*Rufenach, McPherron and Schaper [1992]*). Properties of temperature, velocity  
233 and number density are specified for the ambient species ( $H^+$ ) throughout the domain at  
234 the start of the simulation, and at the inflow boundary for the neutral chemical species.

### 3. Results

235 Simulation results from both steady and unsteady thruster burns are presented in this  
236 section. The first case that is presented examines the ion and neutral steady plume  
237 development without photoionization, such that the ion plume is formed from spacecraft  
238 neutral charge exchange collisions with the ambient  $H^+$ . Recall that charge transfer  
239 between spacecraft neutrals and ambient ions effectively depletes the local ambient plasma  
240 density, and the ambient plasma is assumed to be replenished at a finite rate based on the  
241 time-of-flight of 1 keV  $H^+$  ions from the ambient reservoir at -20 km. As shown in 4(a) and

242 7(a), this is the approximate location at which the neutral plume density drops below the  
243 ambient density. The second case incorporates both charge exchange and photoionization  
244 processes to compare the relative importance of these mechanisms on the formation of the  
245 ion plume. Finally, it is important to note that only the  $\text{H}_2^+/\text{N}_2^+/\text{NH}_3^+$  ions are influenced  
246 by the electrostatic and magnetic field forces; any influence of these forces on the motion  
247 of the neutral  $\text{H}_2/\text{N}_2/\text{NH}_3$  particles is a result of secondary charge-exchange interactions,  
248 in which a neutral particle becomes magnetized through charge-exchange, interacts with  
249 the magnetic field, and then becomes demagnetized through a charge-exchange collision.

250 The second set of simulation results examine an unsteady thruster firing, in which the  
251 thrusters are fired for 2 seconds and then turned off. The evolution of both the neutral  
252 and ion plumes is examined during and after the thruster burn to determine the rate of  
253 dissipation of each chemical species from the computational domain.

### 3.1. Plume Development with Replenished Ambient (RA)

254 The steady-state flow field in the Replenished Ambient (RA) case is presented in Figures  
255 4-6. The contours in Figures 4-6(a) show the number density of the hydrazine neutrals  
256 which are emitted in the  $+x$ -direction from the nozzle exit. The plume undergoes a  
257 strong expansion into the rarefied ambient plasma environment, and these particles in-  
258 teract through MEX and CEX collisions with the ambient ions and with neutral plume  
259 particles. The number density of the corresponding spacecraft ions generated through  
260 charge exchange are shown in 4-6(b). Both neutral and ion plumes undergo expansion in  
261 the near-vacuum ambient, and the ion plume is also subject to forces from the electric  
262 and magnetic fields.

263 Examination of the neutral and ion plumes in Figures 4-6 reveals the influence of the  
264 self-consistent electrostatic field on the ion plume. The neutral chemical species plume un-  
265 dergoes considerable expansion, but the plume generally propagates in the  $+x$ -direction.  
266 The plume concentrations in the farfield remain orders of magnitude higher than the am-  
267 bient density, which is represented by the lower saturation of the contour levels at  $1.0 \times 10^6$   
268  $\text{m}^{-3}$ . Owing to the plume composition and relatively small molecular mass, the  $\text{H}_2$  plume  
269 shows the greatest extent while the  $\text{N}_2$  and  $\text{NH}_3$  plumes are at lower concentrations.

270 The corresponding ion plumes are significantly lower in density, and the ion plume  
271 concentration is limited to values near or below the ambient density. This is due to the  
272 depleting nature of the  $\text{H}^+$  ions from charge exchange collisions; the finite-rate replenishing  
273 of the ambient ions in the path of the neutral plume is significantly longer than the charge  
274 exchange collision frequency between the neutral particles and ambient ions. As a result,  
275 the ion plume concentration in this case is limited by the ambient ions available for charge  
276 exchange.

277 The evolution of the ion plumes indicates a strong influence of the electric field on the  
278 charged chemical speices. The acceleration due to the electrostatic forces drive the ions  
279 away from the thruster origin, both in the upstream ( $-x$ ,  $\text{H}^+_{2}$  only) and downstream  
280 ( $+x$ ) directions. In each case, the ion plume concentration is significantly higher in the  
281 downstream direction; this is attributed to the higher concentration of neutral plume  
282 chemical species downstream available for ion plume production. The significant spread  
283 of the ion plume however underscores the influence of the electrostatic field on the ion  
284 plumes.

### 3.2. Plume Development with Photoionization (PI)

285 The steady-state flow field generated with a Replenished Ambient (RA) and Photoion-  
286 ization (PI) is presented in Figures 7-9(a) and Figures 7-9(b). The contours in Figures  
287 7-9(a) again show the hydrazine neutral number density. Recall that in this case the  
288 spacecraft neutrals may undergo charge exchange with the ambient  $H^+$  ions, and may also  
289 undergo photoionization. The number density of the spacecraft ions generated through  
290 charge exchange are shown in Figures 7-9(b). The neutral plume development is nearly  
291 identical to the plumes presented in the previous section, and develop largely in the  
292  $+x$ -direction. The ion plumes, however, show a significant increase in concentration ow-  
293 ing to the additional ion production through photoionization. Although the majority of  
294 the  $N^+_2$  and  $NH^+_3$  ion plumes remains at a concentration below the ambient density, the  
295  $H^+_2$  ion plume has a high-density core that extends 15 km downstream of the thruster  
296 origin.

297 A quantitative comparison of the results from Figures 5-9 is presented in Figure 10(a)-  
298 (c). These figures show the number density of the spacecraft neutrals ( $H_2, N_2, NH_3$ ) and  
299 ions ( $H^+_2, N^+_2, NH^+_3$ ) along the plume centerline, starting from the thruster exit, in the  
300  $+x$ -direction. The solid lines indicate the number density of the spacecraft neutrals as  
301 a function of distance from the thruster, and the dashed lines represent the spacecraft  
302 ions. Number density profiles are shown for three distinct simulation cases: (i) RA, the  
303 Replenished Ambient case, and (ii) PI, the Photoionization case including Replenished  
304 Ambient (both presented above), and (iii) FA, the Fixed Ambient case (not reprinted  
305 above). The Fixed Ambient case assumes that the ambient  $H^+$  ions are replenished at an  
306 infinite rate, providing a fixed ambient density for charge exchange processes throughout  
307 the simulation. It is observed in these comparisons that photoionization has a significant

308 impact on the ion plume concentration, increasing the ion plume density by approximately  
309 one order of magnitude. As shown by this comparison, the increase in ion concentration  
310 is approximately equivalent to assuming an infinite replenishing rate (or Fixed Ambient)  
311 for the ambient ions.

### 3.3. Unsteady plume simulations

312 Plume simulation results are presented next which examine an unsteady thruster plume  
313 firing for two seconds, after which the thrusters are turned off. The thrusters fire in the  
314  $+x$ -direction, and the neutral plume expands in the near-vacuum ambient while under-  
315 going charge exchange and photoionization. The simulation results show the convection  
316 and eventual dissipation of the neutral and ion plumes to levels below the ambient density  
317 of approximately  $1 \times 10^6 \text{ m}^{-3}$  for each of the chemical species. Each column in Figure  
318 11 represents the time evolution of the neutral plumes (black contour lines) and the ion  
319 plumes (red contour lines), starting at two seconds (top row) and stepping through time  
320 up until the majority of the plume has convected out of the domain (bottom row).

321 The total time required for the neutral and ion plumes to dissipate to levels below the  
322 ambient density everywhere ( $\pm 35$  km from the spacecraft) is approximately 34 seconds.  
323 The core of the neutral plume (the highest density region) leaves the computational do-  
324 main after approximately 15 seconds, which is the time required for a plume traveling at  
325 the thruster exit velocity of 1900 m/s to reach the edge of the computational domain. As  
326 the plume is comprised of chemical species which vary in molecular weight, the lighter  
327 plume species are faster and the core of the  $\text{H}_2$  plume reaches the edge of the domain first,  
328 followed by the  $\text{NH}_3$  and then the  $\text{N}_2$  plume core. This ‘time of flight’ is nearly half of  
329 the total dissipation time. The additional time required for dissipation is largely a result

330 of the plume expansion, as well as collisional effects near the thruster exit. These mecha-  
331 nisms work to decrease or reverse the plume neutral particle velocities such that the edges  
332 of the plume remain within the computational domain for an extended period after the  
333 core of the plume has already vanished. It is found that the  $N_2$  plume vanishes completely  
334 (below the ambient number density levels) first, after approximately 26 seconds, while the  
335  $H_2$  is the final chemical species to dissipate completely.

#### 4. Conclusions

336 The focus of this work was to examine the development of spacecraft neutral and ion  
337 plumes during steady and unsteady hydrazine thruster burns. The plume was modeled as  
338 a gas mixture comprised of the primary hydrazine post-combustion products, consisting  
339 of  $H_2$ ,  $N_2$  and  $NH_3$ , subject to interaction with the ambient  $H^+$  ions in the magnetosphere  
340 and photoionization. Detailed differential and total cross sections were used to model  
341 the formation of spacecraft ions formed during charge exchange (CEX) interactions with  
342 ambient ions in the magnetosphere plasma. This work also established the relative sig-  
343 nificance of the competing mechanisms of charge exchange ( $H^+$  depletion) and ambient  
344 replenishing within the plume, as well as photoionization processes. Both steady and  
345 unsteady spacecraft neutral and ion plume results were presented.

346 The neutral plumes generated from the hydrazine rocket were not strongly influenced by  
347 the selection of the ionization mechanisms (i.e., charge exchange with or without photoion-  
348 ization), as the neutral plume densities and general shapes were nearly identical in the two  
349 cases. The ion plumes, however, showed a significant increase in both concentration and  
350 extent, when photoionization is included. The concentration along the plume centerline  
351 was increased by approximately one order of magnitude, which was found to be approxi-

352 mately equivalent results employing the Fixed Ambient model (infinite replenishing rate)  
353 without photoionization.

354 The unsteady simulation of the two-second thruster burn examined the relative neutral  
355 and ion plume convection and dissipation at large distances ( $\pm 35$  km) from the spacecraft.  
356 The ion plume, although present at lower concentrations, closely tracked the high-density  
357 neutral core. The densities drop to values below the ambient, with only traces of low  $H_2$   
358 plume concentrations ( $O(10^6) \text{ m}^{-3}$ ) near the plume centerline after 33 seconds.

359 **Acknowledgments.** The support of Air Force Research Laboratory (AFRL) Space  
360 Vehicles Directorate and Barron Associates, Inc. for this work under subcontract FA9453-  
361 11-C-0181 is gratefully acknowledged. The authors are also grateful for the helpful sug-  
362 gestions by the reviewers. Information regarding the simulation results presented in this  
363 paper may be obtained from K. Stephani. Computational resources and technical support  
364 were provided by the CAEN Advanced Computing Center at the University of Michigan,  
365 and by the Texas Advanced Computing Center through a National Science Foundation  
366 XSEDE award.

## References

- 367 Alexeenko, A., D. Wadsworth, S. Gimelshein, and A. Ketsdever (2004), Numerical Model-  
368 ing of ISS Thruster Plume Induced Contamination Environment, *Optical System Con-*  
369 *tamination: Effects, Measurements and Control VII Conference (AM405), SPIE 49th*  
370 *Annual Meeting*.
- 371 Bernhardt, P., J. Ballenthin, J. Baumgardner, A. Bhatt, I. Boyd, J. Burt, R. Caton,  
372 A. Coster, P. Erickson, J. Huba, G. Earle, C. Kaplan, J. Foster, K. Groves, R. Haaser,

- 373 R. Hellis, D. Hunton, D. Hysell, J. Klenzing, M. Larsen, F. Lind, T. Pedersen,  
374 R. Pfaff, R. Stoneback, P. Roddy, S. Rodriguez, G. San Antonio, P. Schuck, C. Sieftring,  
375 C. Selcher, S. Smith, J. Talaat, E.R. Thomason, R. Tsunoda, and R. Varney (2012),  
376 Ground and Space-based Measurement of Rocket Engine Burns in the Ionosphere, *IEEE*  
377 *Trans. Plasma Sci.*, 40(5).
- 378 Bird, G. (1994), *Molecular Gas Dynamics and the Direct Simulation of Gas Flows*, Oxford  
379 University Press, Oxford.
- 380 Birdsall, C., and A. Langdon (2004), *Plasma Physics via Computer Simulation*, Taylor  
381 and Francis, New York.
- 382 Burke, W., L. Gentile, J. Machuzak, D. Hardy, and D. Hunton (1995), Energy Distribu-  
383 tions of Thruster Pickup Ions Detected by the Shuttle Potential and Return Electron  
384 Experiments during TSS 1, *J. Geophys. Res.*, 100(A10).
- 385 Cabrera-Trujillo, R., Y. Ohrn, E. Deumens, J. Sabin, and B. Lindsay (2002), Theoretical  
386 and experimental studies of the  $H^+-N_2$  system: Differential cross sections for direct and  
387 charge-transfer scattering at kilo-electron-volt energies, *Physical Review A*, 66(042712).
- 388 Cai, C. (2005), *Theoretical and Numerical Studies of Plume Flows in Vacuum Chambers*,  
389 Ph.D. Dissertation, University of Michigan, Ann Arbor, MI.
- 390 Coplan, M. and K. Ogilvie (1970), Charge Exchange for  $H^+$  and  $H_2^+$  in  $H_2O$ ,  $CO_2$ , and  
391  $NH_3$ , *J. Chem. Phys.*, 52(4154).
- 392 Drakes, J., and D. Swann (1999), DSMC Computations of the Progress-M Spacecraft  
393 Retrofiring Exhaust Plume, *AIAA Paper No. AIAA-99-0975*.
- 394 Kaplan, C., and P. Bernhardt (2010), Effect of an Altitude-dependent Background Atmo-  
395 sphere on Shuttle Plumes, *J. Spacecraft and Rockets*, 47(4).



- 396 Karabadzhak, G., Y. Plastinin, B. Khmelinin, V. Teslenko, N. Shvets, J. Drakes,  
397 D. Swann, and W. McGregor (1997), Experimentation Using the Mir Station as a  
398 Space Laboratory, *AIAA Paper No. AIAA-97-0288*.
- 399 Kusakabe, T., A. Kensuke, J. Gu, G. Hirsch, R. Buenker, M. Kimura, J. Tawara, and  
400 Y. Nakai, (2000), Charge-transfer processes in collisions of H<sup>+</sup> ions with H<sub>2</sub>, D<sub>2</sub>, CO  
401 and CO<sub>2</sub> molecules in the energy range 0.2-4.0 keV, *Physical Review A*, 62(062714).
- 402 McMahon, W., R. Salter, R. Hills, and D. Delorey (1983), Measured electron contribution  
403 to shuttle plasma environment, *AIAA Paper No. AIAA-83-2598*.
- 404 Ngalande, C., T. Lilly, M. Killingsworth, S. Gimelshein, and A. Ketsdever (2006), Nozzle  
405 Plume Impingement on Spacecraft Surfaces: Effects of Surface Roughness, *J. Spacecraft*  
406 *Rockets*, 43, 5.
- 407 Rufenach, C., R. McPherron, and J. Schaper (1992), The Quiet Geomagnetic Field at  
408 Geosynchronous Orbit and Its Dependence on Solar Wind Dynamics Pressure, *J. Geo-*  
409 *phys. Res.*, 97(A1), 2101-2116.
- 410 Stephani, K., and I. Boyd (2014), Detailed Modeling and Analysis of Spacecraft  
411 Plume/Ionosphere Interactions in Low Earth Orbit, *J. Geophys. Res. - Space*, 119,  
412 2101-2116.
- 413 Stephani, K., I. Boyd, R. Balthazor, M. McHarg, B. Mueller, and R. Adams (2014),  
414 Analysis and observation of spacecraft plume/ionosphere interactions during maneuvers  
415 of the space shuttle, *J. Geophys. Res. - Space*, 119, 7636-7648.
- 416 Yim, J., F. Sibé, and N. Ierardo (2014), Plume Impingement Analysis for the European  
417 Service Module Propulsion System, *50th AIAA/ASME/SAE/ASEE Joint Propulsion*  
418 *Conference*.

**Table 1.** VHS parameters for  $\text{H}_2/\text{N}_2/\text{NH}_3$ 

	$d_{ref}$	$T_{ref}$	$\omega$
$\text{H}_2$	2.92Å	273K	0.75
$\text{N}_2$	4.17Å	273K	0.75
$\text{NH}_3$	5.94Å	273K	0.75

**Figure 1.** Transformation from LAB→CM frame of reference for particles of different mass.**Figure 2.** (a) Differential cross sections (DCS) and (b) total cross sections (TCS) for collision dynamics of  $\text{H}_2/\text{N}_2/\text{NH}_3 - \text{H}^+$  system.**Figure 3.** DSMC/PIC computational domain. Axis of symmetry lies along the x-axis, and the nozzle exit plane is located at the origin. Red arrow indicates the plume flow direction, and geomagnetic field lines are aligned with the z-axis.

**Table 2.** Thruster Exit Plane Conditions and Ambient Flow Conditions

Species	m [kg kmol <sup>-1</sup> ]	k <sub>b</sub> T/q <sub>0</sub> [eV]	V [m s <sup>-1</sup> ]	n [m <sup>-3</sup> ]
H <sub>2</sub>	2.02	0.03	1900	3.99 × 10 <sup>23</sup>
N <sub>2</sub>	28.0	0.03	1900	1.74 × 10 <sup>22</sup>
NH <sub>3</sub>	17.0	0.03	1900	1.99 × 10 <sup>22</sup>
H <sup>+</sup>	1.01	1.0 × 10 <sup>3</sup>	0	3.0 × 10 <sup>6</sup>

**Table 3.** Larmor Radius (with B-field variation)

Species	mean [km]	variation (+/-)
r <sub>L,H<sub>2</sub></sub>	0.4	0.30/0.46
r <sub>L,N<sub>2</sub></sub>	5.6	4.2/6.5
r <sub>L,NH<sub>3</sub></sub>	3.3	2.6/4.0

**Figure 4.** Contours of (a) H<sub>2</sub> number density and (b) H<sub>2</sub><sup>+</sup> number density for charge exchange with a Replenished Ambient (RA). The lower saturation limit on the contour levels correspond to the ambient density. Note the difference in the contour level upper limits.

**Figure 5.** Contours of (a)  $N_2$  number density and (b)  $N_2^+$  number density for charge exchange with a Replenished Ambient (RA). The lower saturation limit on the contour levels correspond to the ambient density. Note the difference in the contour level upper limits.

**Figure 6.** Contours of (a)  $NH_3$  number density and (b)  $NH_3^+$  number density for charge exchange with a Replenished Ambient (RA). The lower saturation limit on the contour levels correspond to the ambient density. Note the difference in the contour level upper limits.

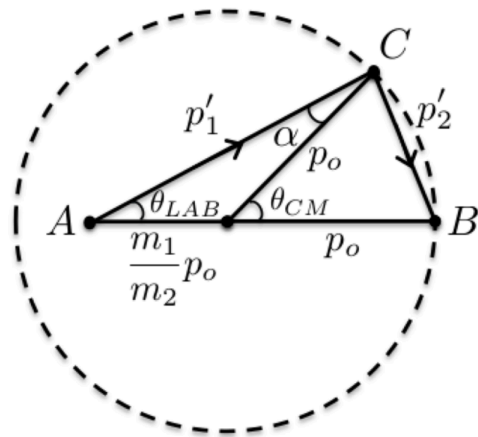
**Figure 7.** Contours of (a)  $H_2$  number density and (b)  $H_2^+$  number density for photoionization (PI) with a Replenished Ambient (RA). The lower saturation limit on the contour levels correspond to the ambient density. Note the difference in the contour level upper limits.

**Figure 8.** Contours of (a)  $N_2$  number density and (b)  $N_2^+$  number density for photoionization (PI) with a Replenished Ambient (RA). The lower saturation limit on the contour levels correspond to the ambient density. Note the difference in the contour level upper limits.

**Figure 9.** Contours of (a)  $\text{NH}_3$  number density and (b)  $\text{NH}_3^+$  number density for photoionization (PI) with a Replenished Ambient (RA). The lower saturation limit on the contour levels correspond to the ambient density. Note the difference in the contour level upper limits.

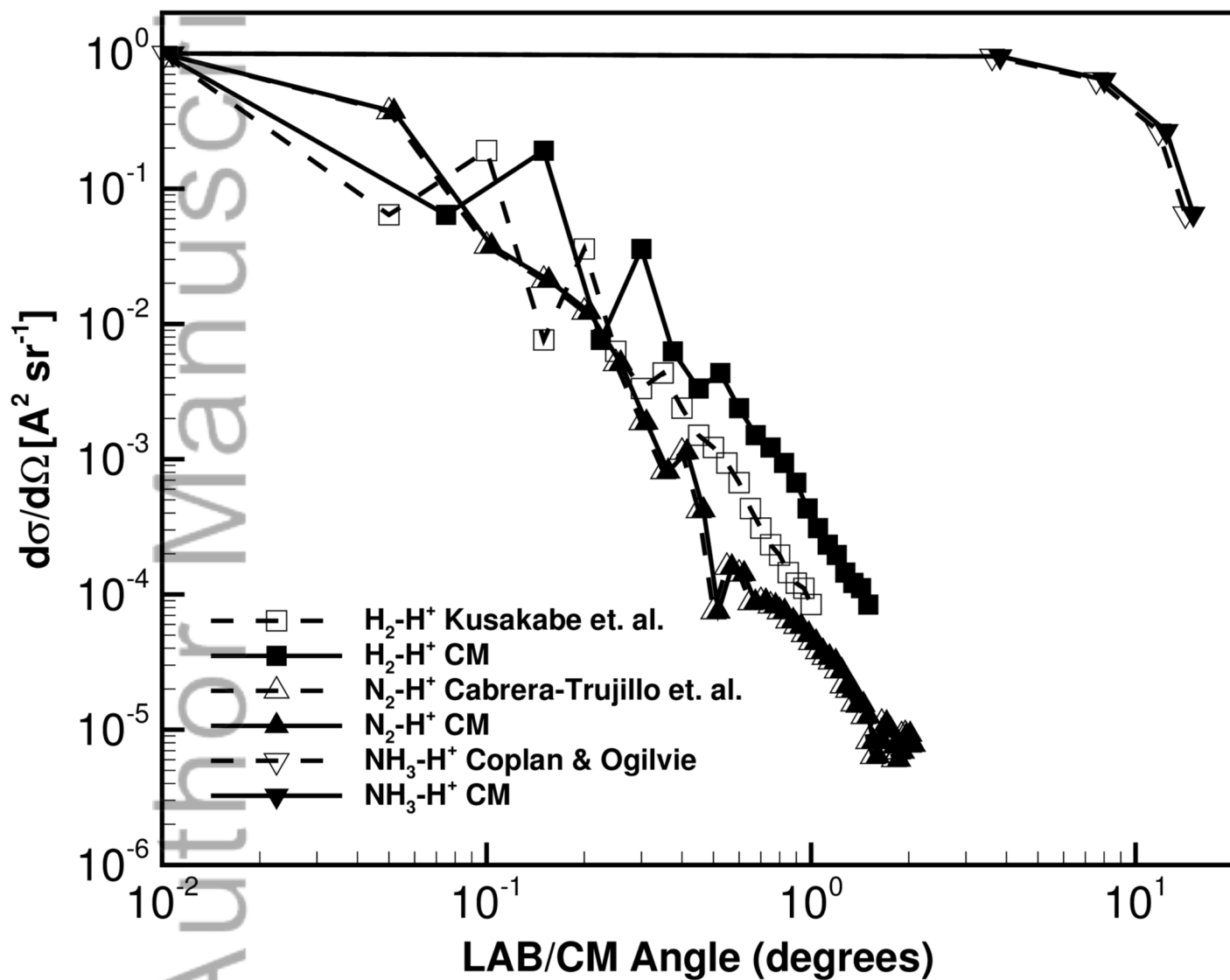
**Figure 10.** Plots of (a)  $\text{H}_2/\text{H}^+_{2}$ , (b)  $\text{N}_2/\text{N}^+_{2}$  number density, and (c)  $\text{NH}_3/\text{NH}^+_{3}$  number density for Fixed Ambient (FA), Replenished Ambient (RA), and photoionization (PI) with a Replenished Ambient (RA) along the plume centerline as a function of  $x$ .

**Figure 11.** Time evolution of neutral and ion plumes during an unsteady thruster firing with  $B=1.1 \times 10^{-7}$  T, with replenishing and photoionization. Thrusters are fired for 2.0 seconds (top row) and then turned off. The lightest of the species,  $\text{H}_2$  exhibits the greatest plume diffusion, while the heaviest of the species,  $\text{NH}_3$  convects out of the computational domain first.

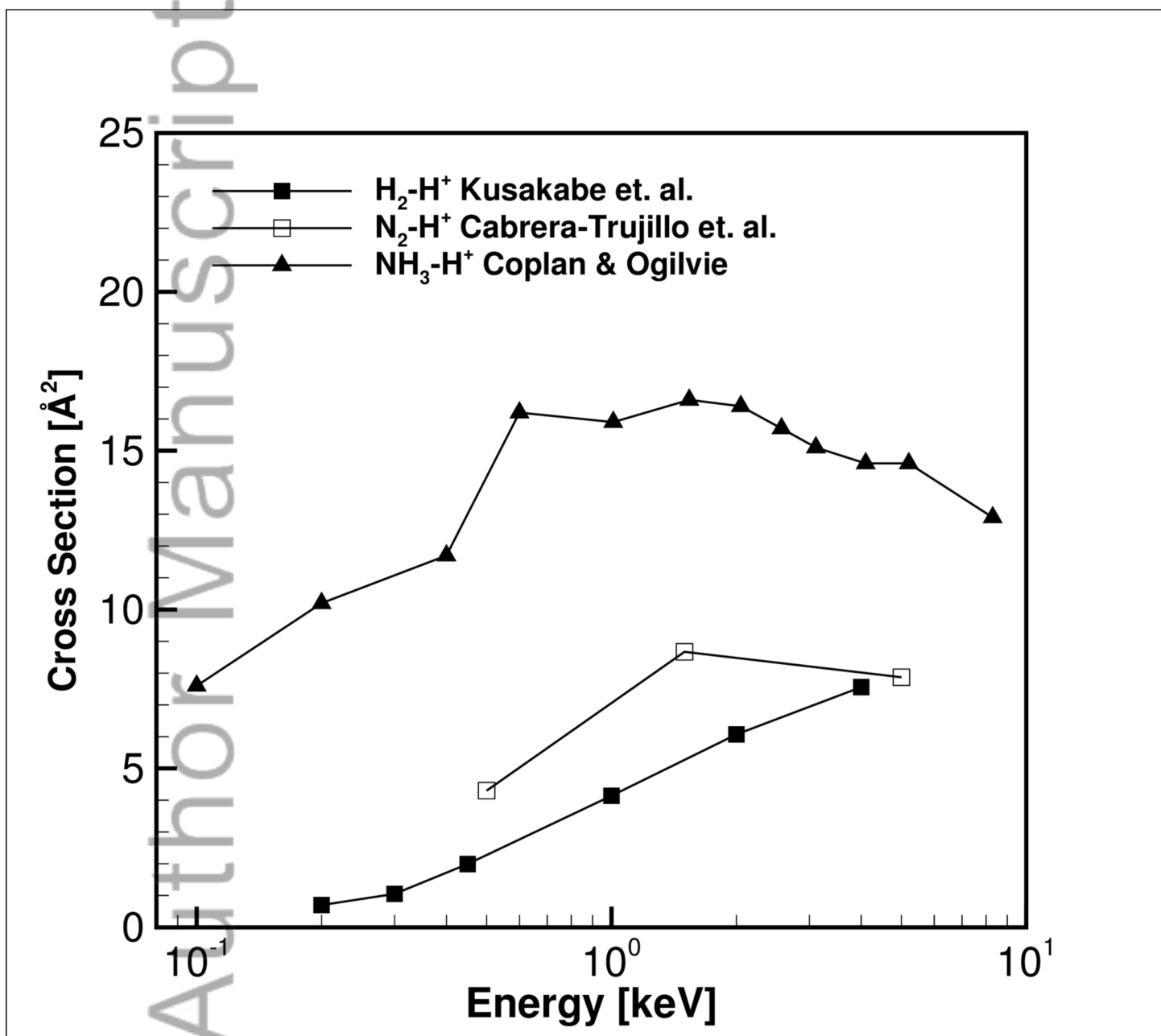


2015ja021158-f00-z-bw

Author Manuscript

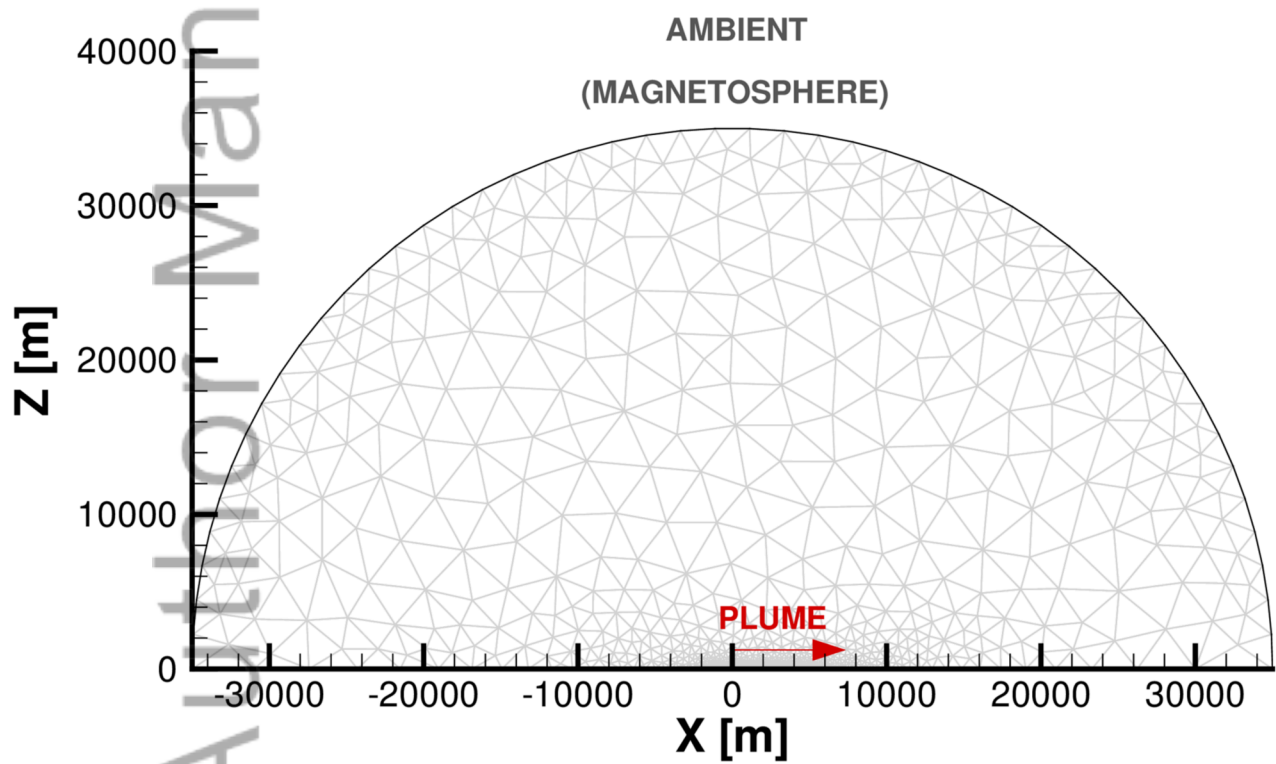


2015ja021158-f01-z-bw

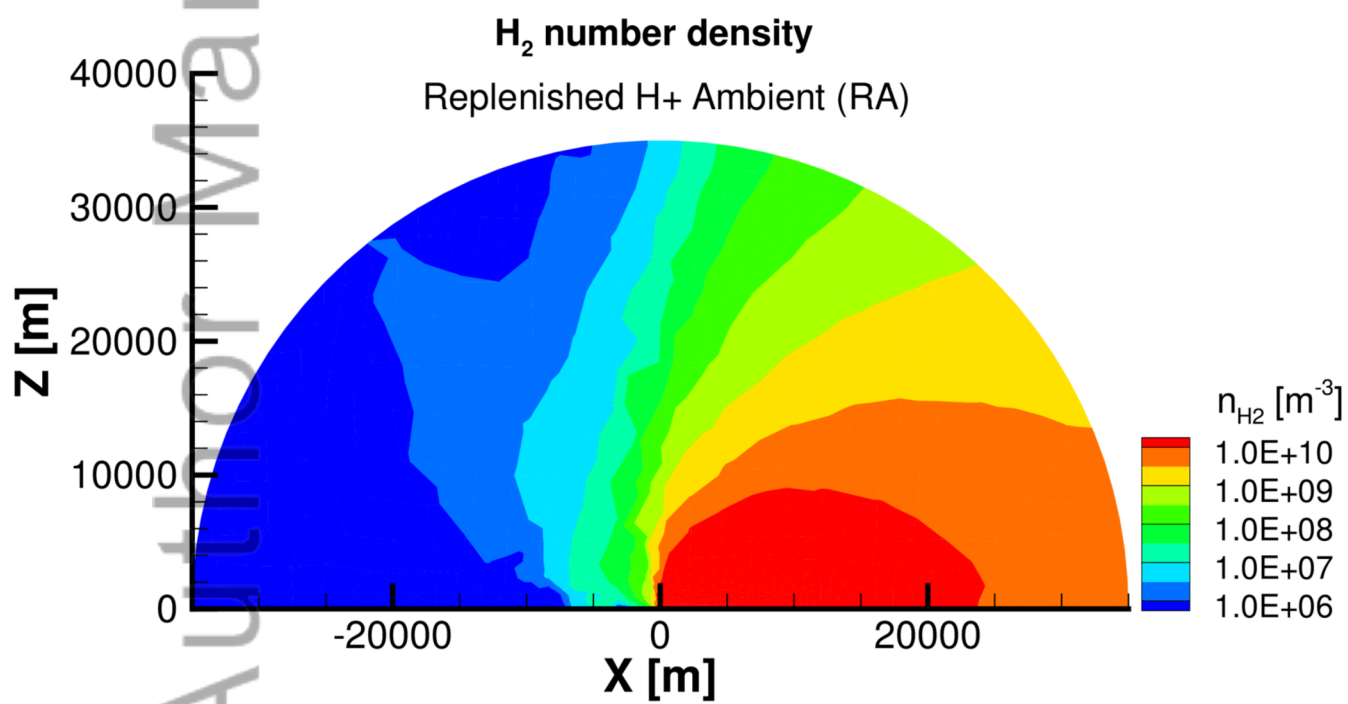


2015ja021158-f02-z-bw

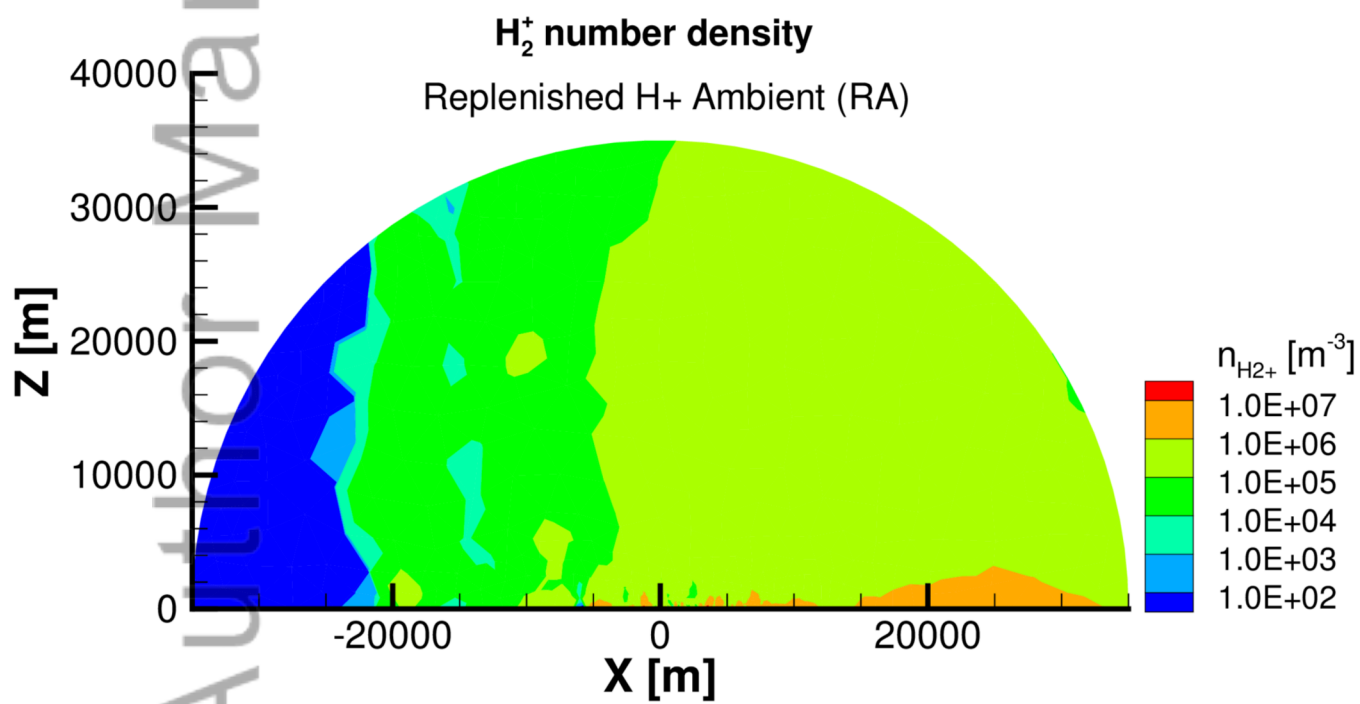




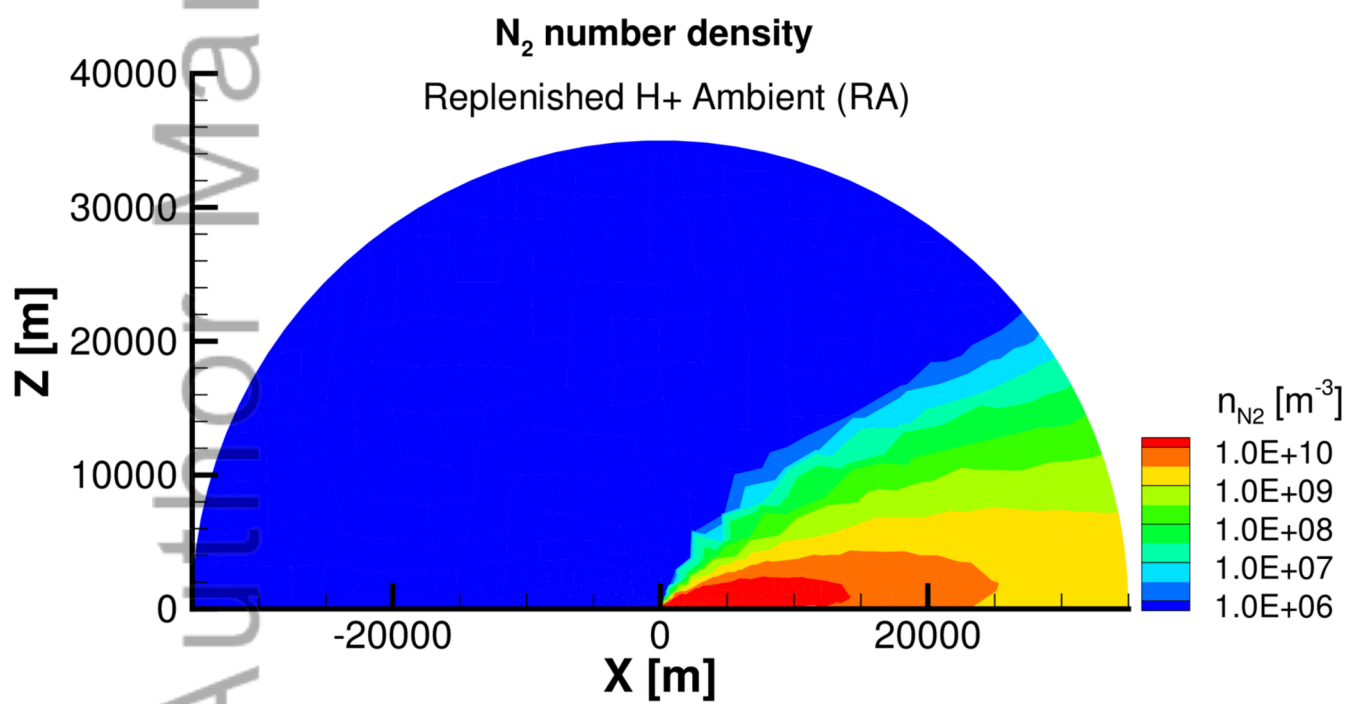
2015ja021158-f03-z-



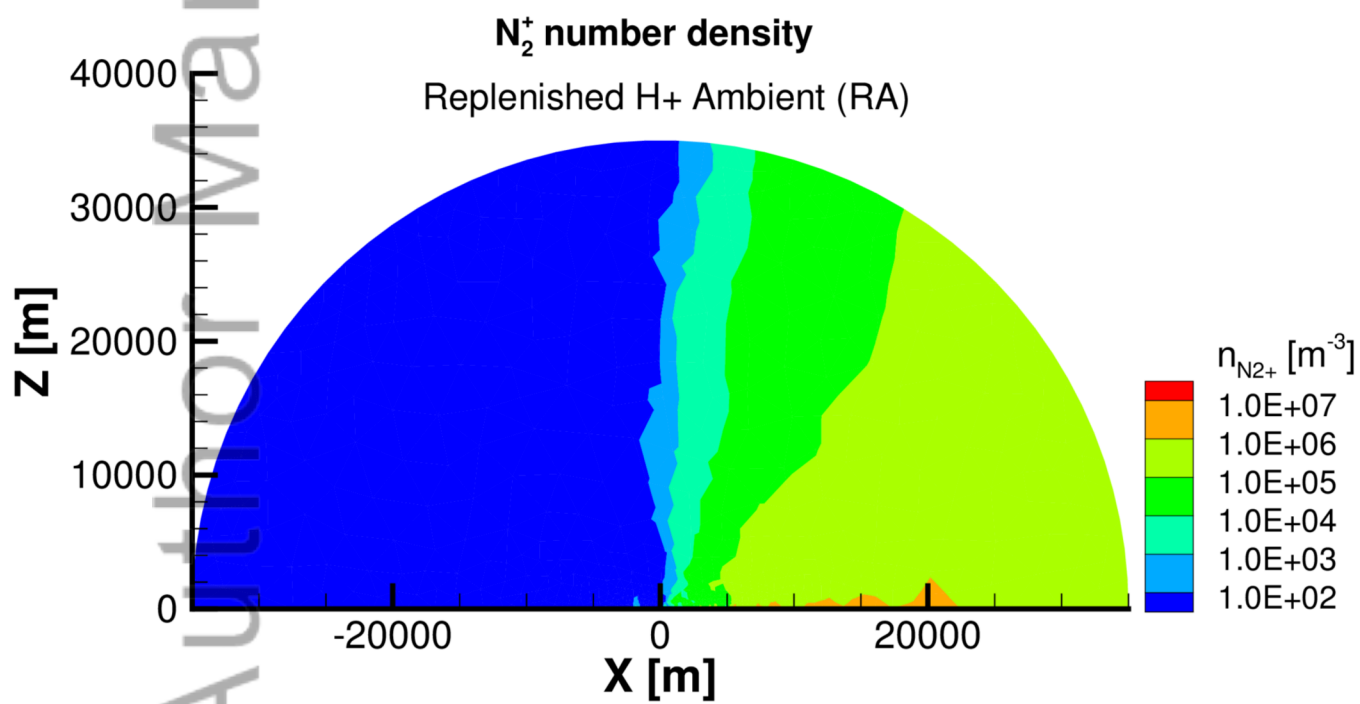
2015ja021158-f04-z-



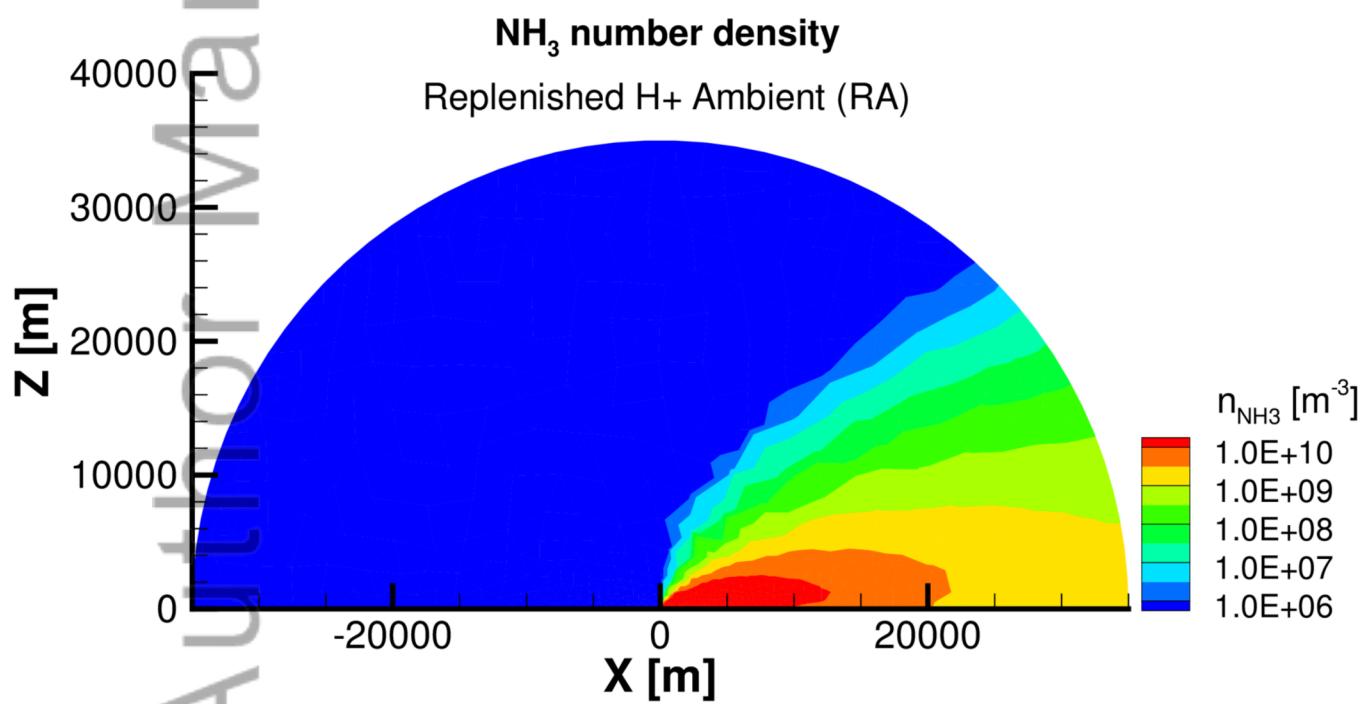
2015ja021158-f05-z-



2015ja021158-f06-z-

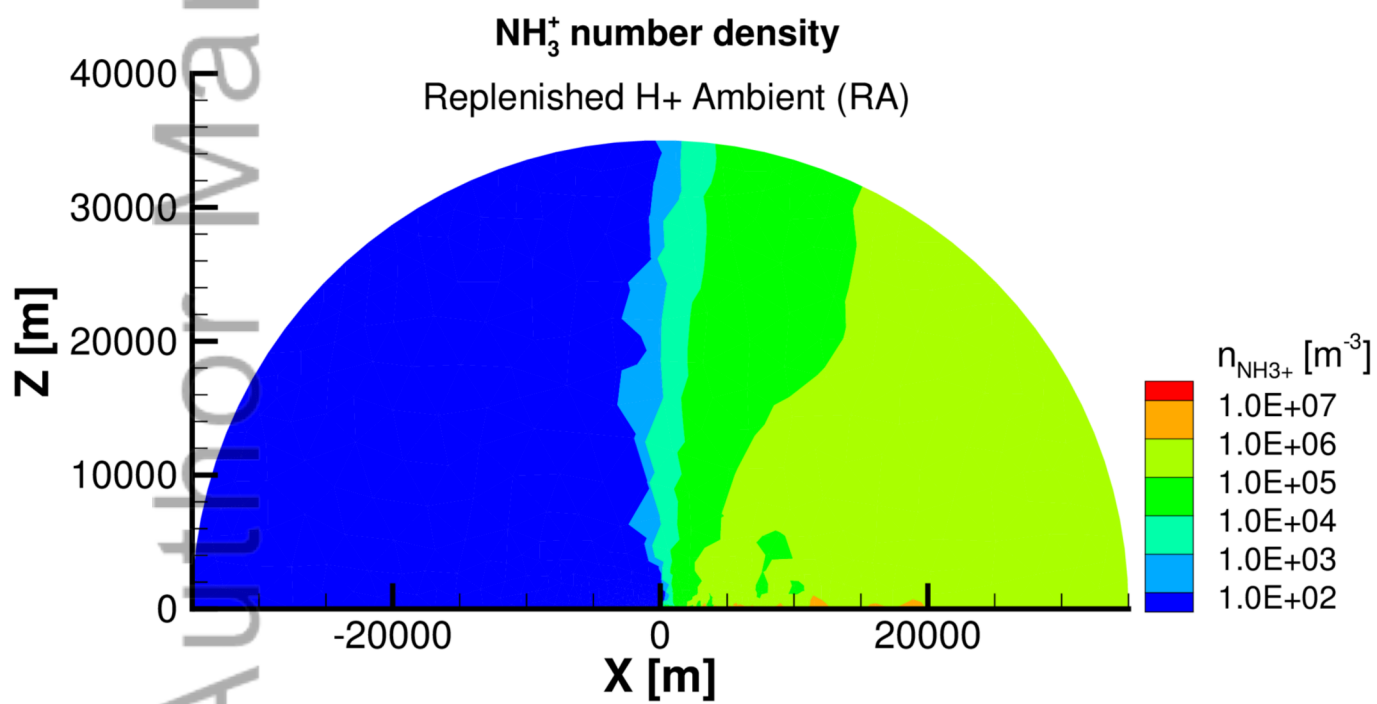


2015ja021158-f07-z-

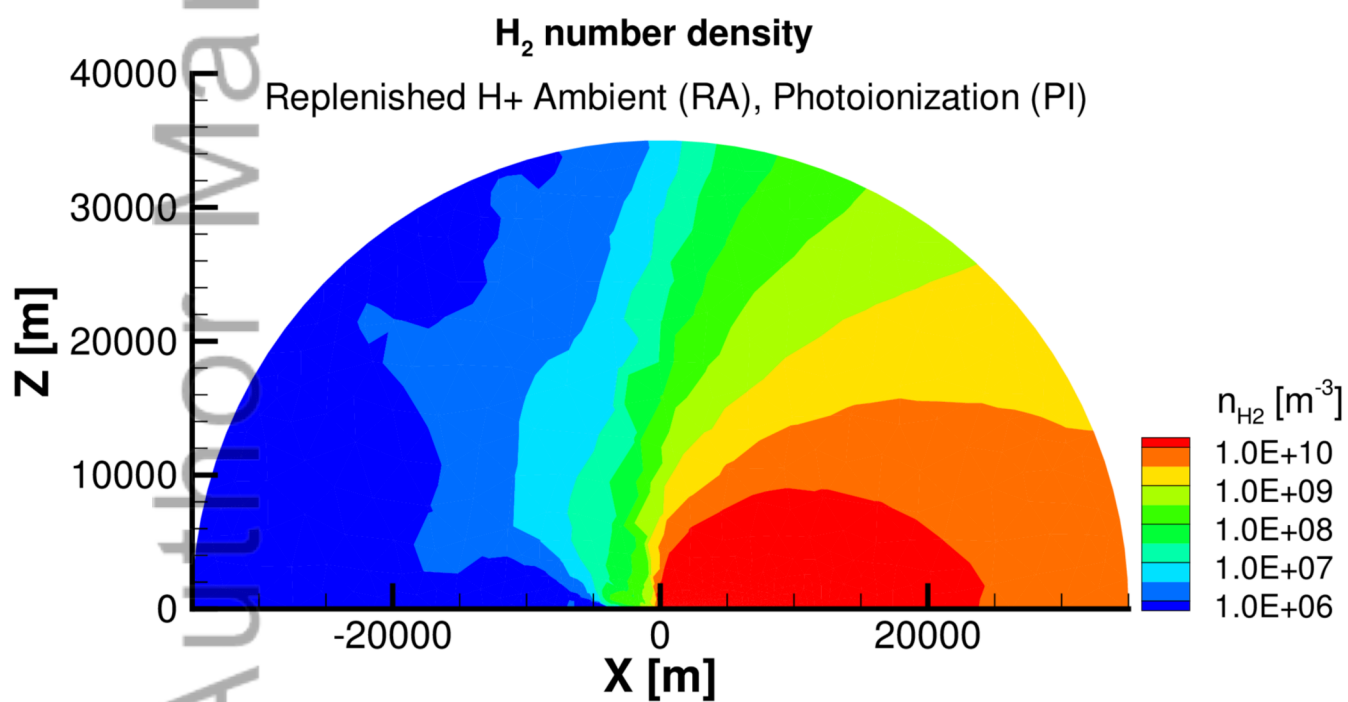


2015ja021158-f08-z-

Author Manuscript

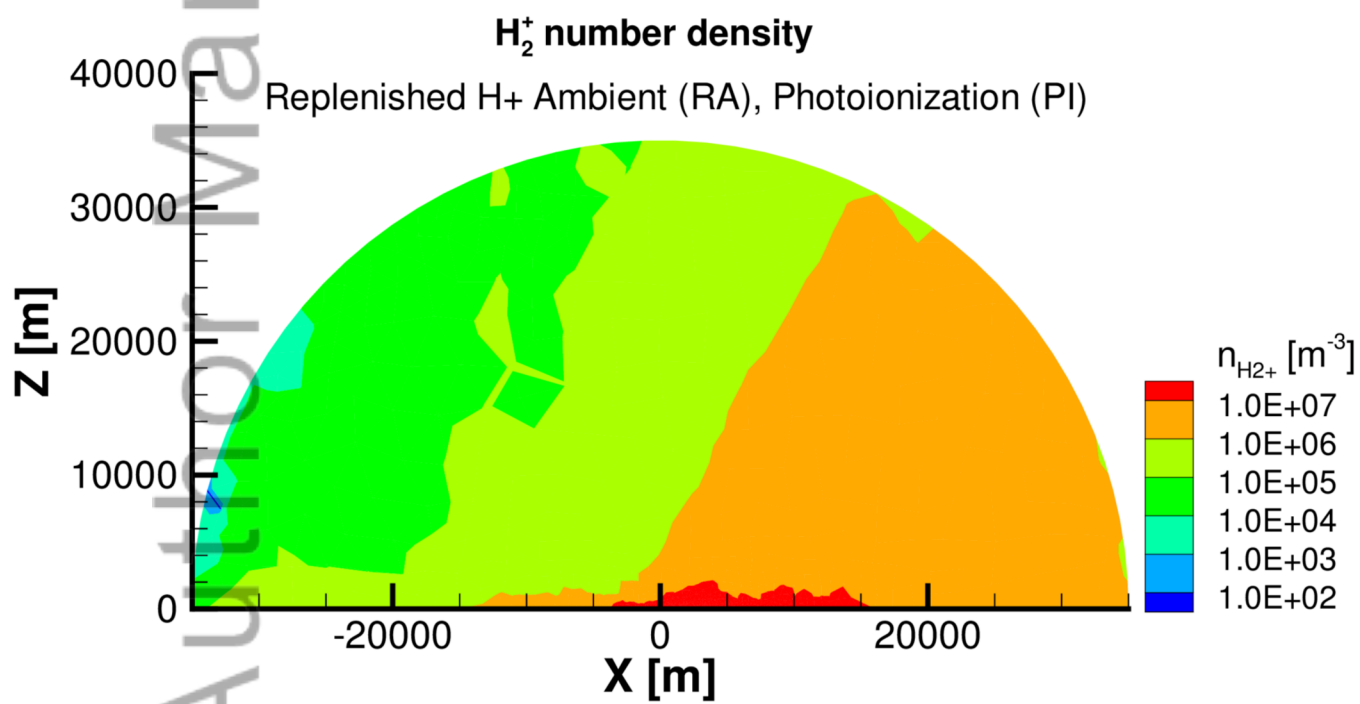


2015ja021158-f09-z-

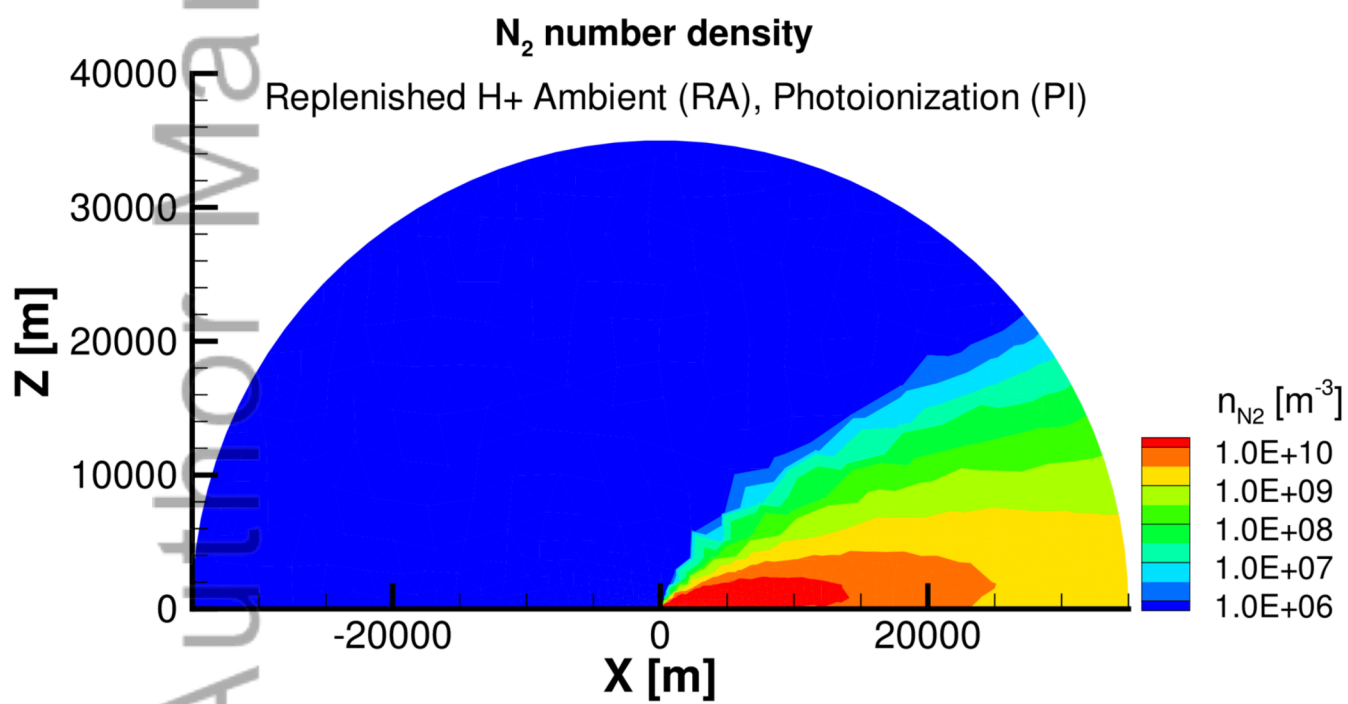


2015ja021158-f10-z-

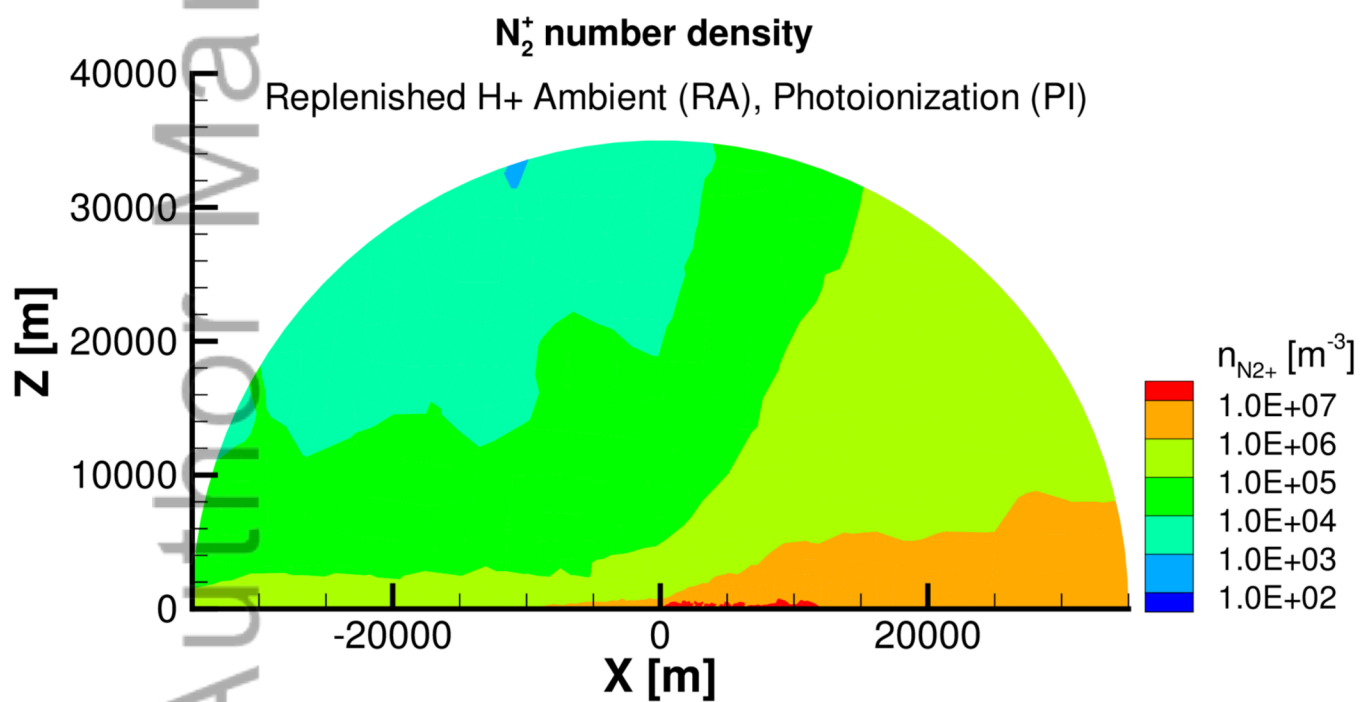




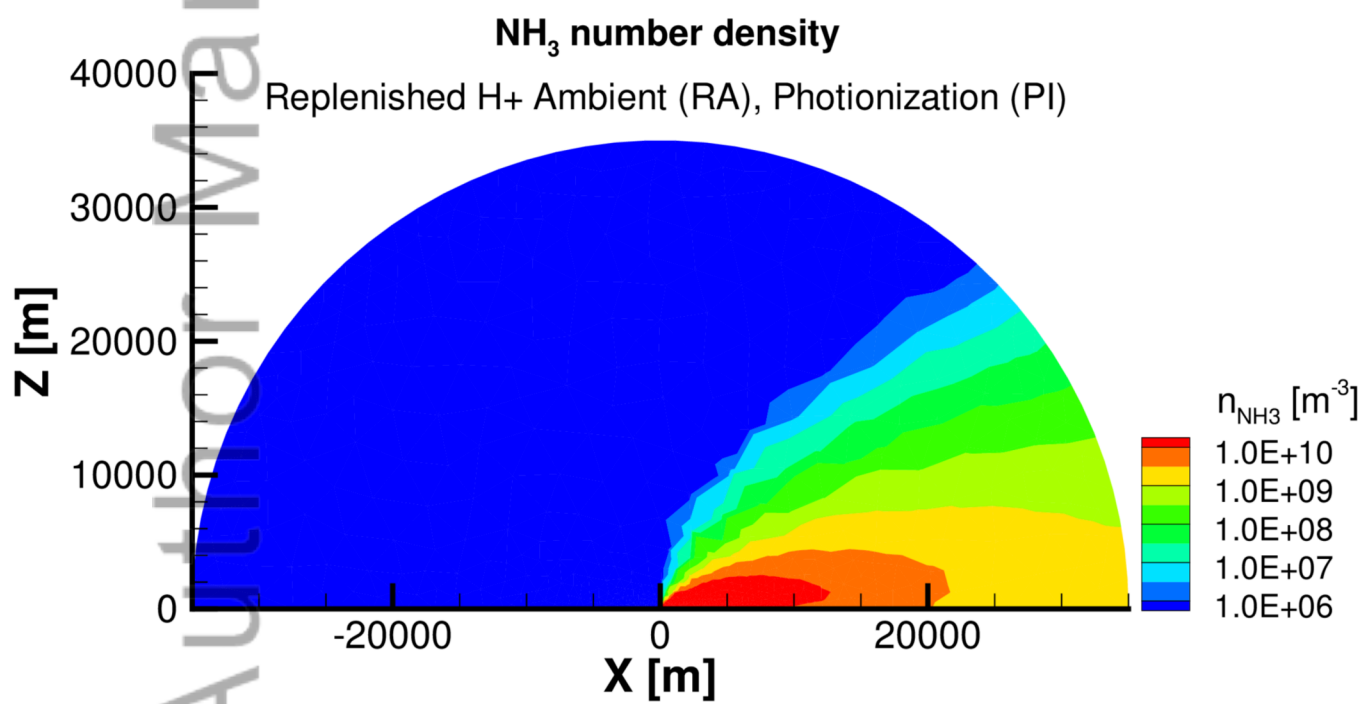
2015ja021158-f11-z-



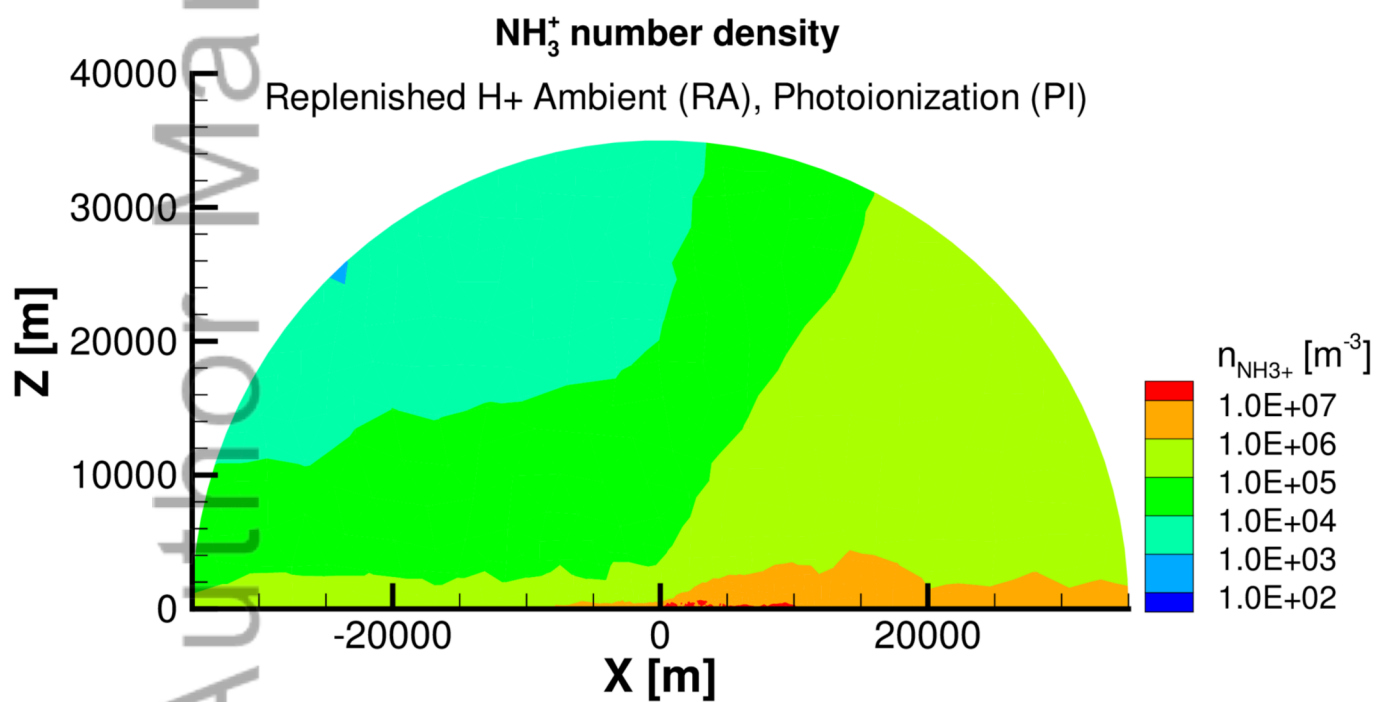
2015ja021158-f12-z-



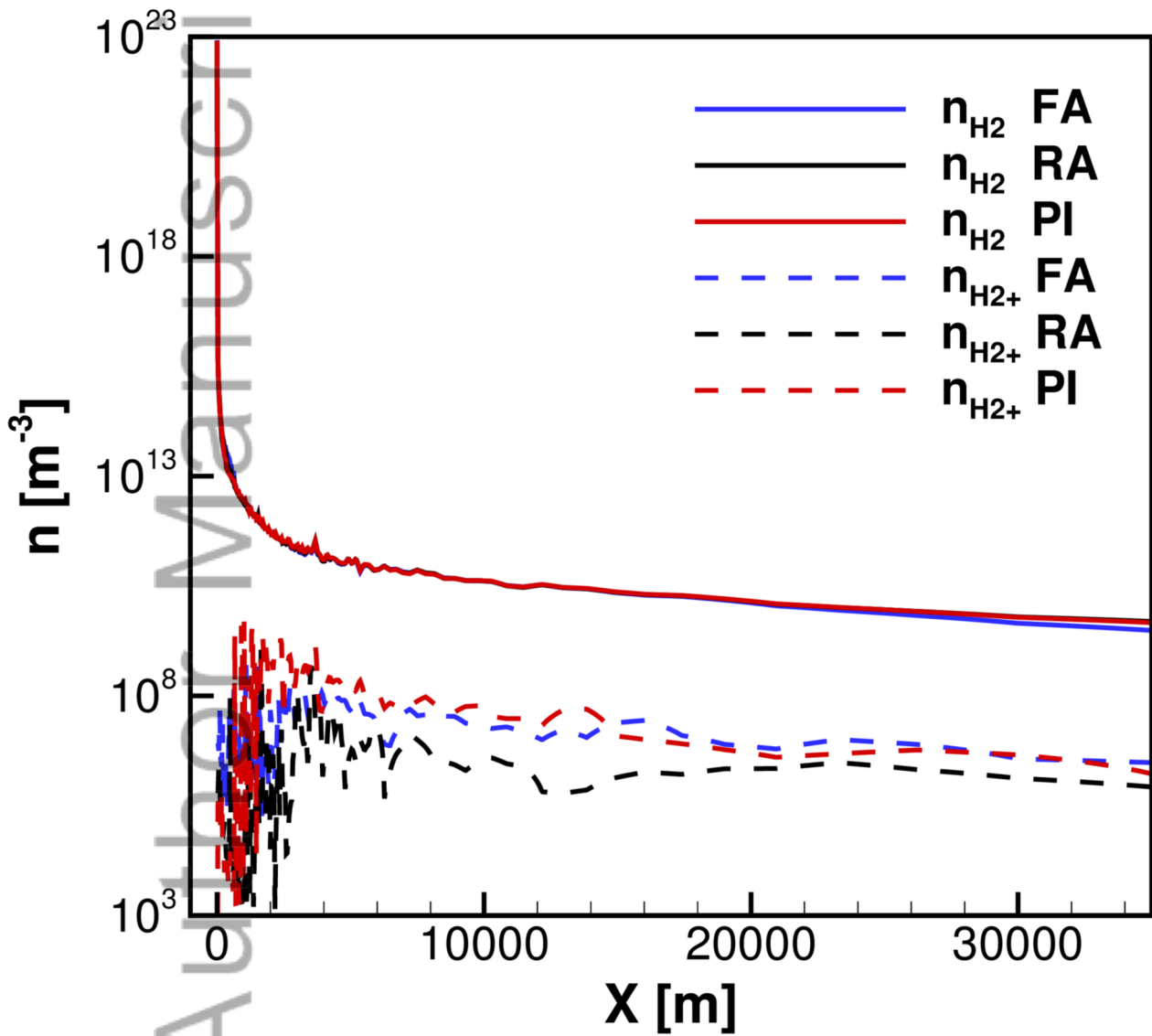
2015ja021158-f13-z-



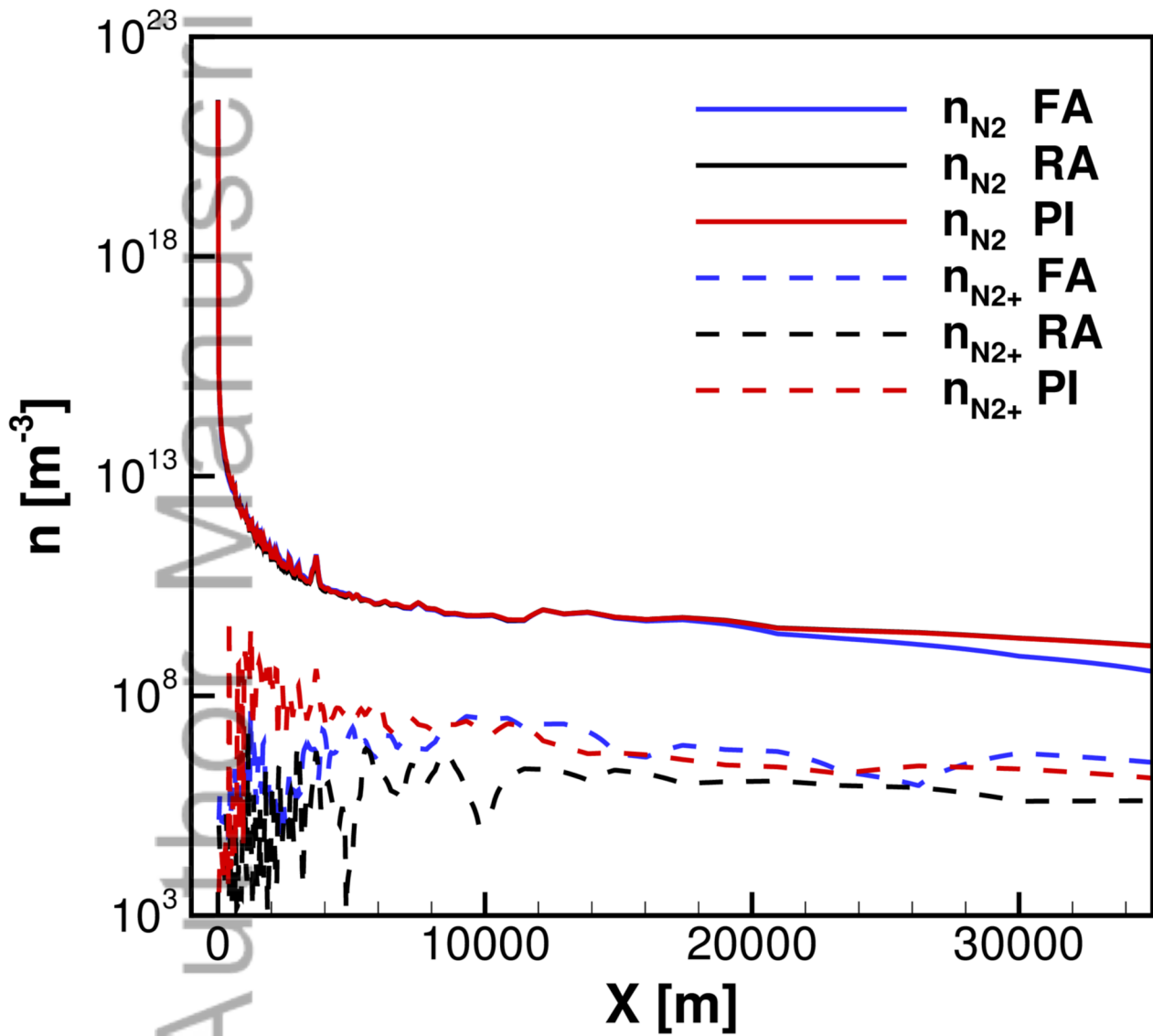
2015ja021158-f14-z-



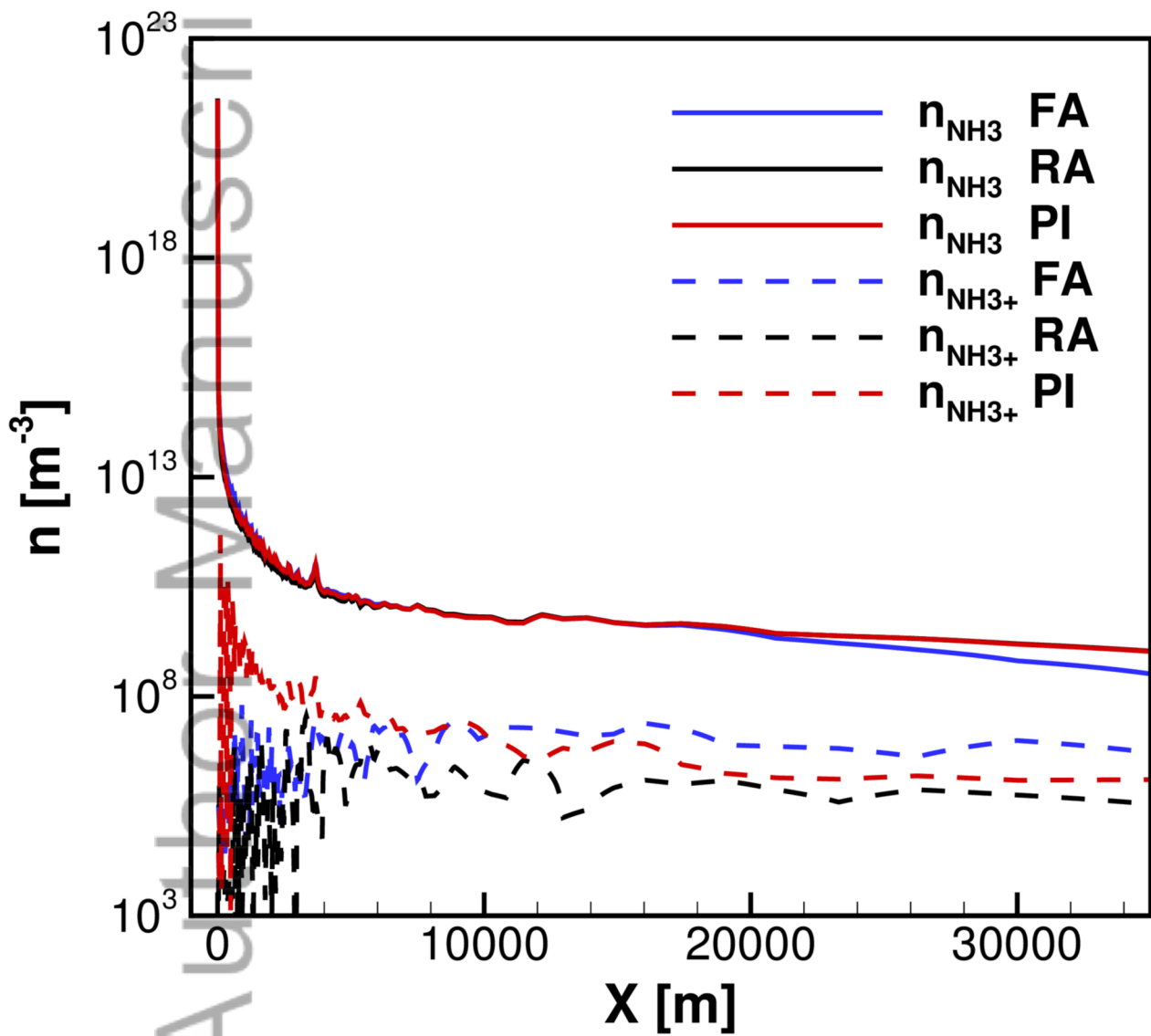
2015ja021158-f15-z-



2015ja021158-f16-z-

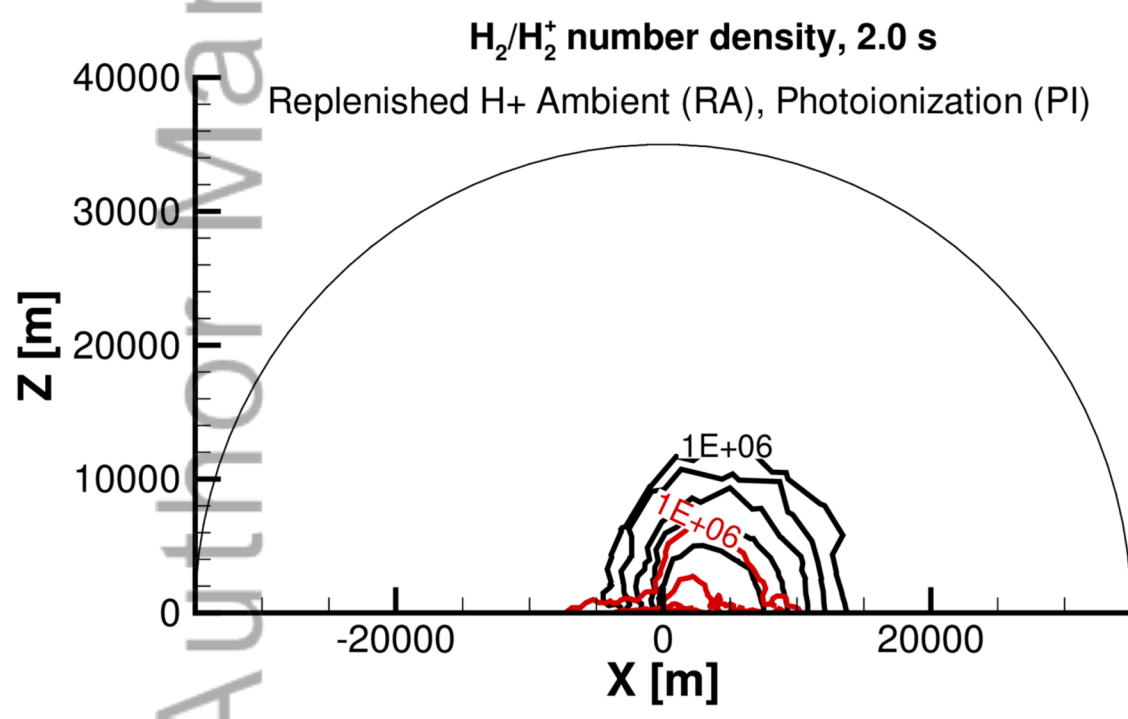


2015ja021158-f17-z-

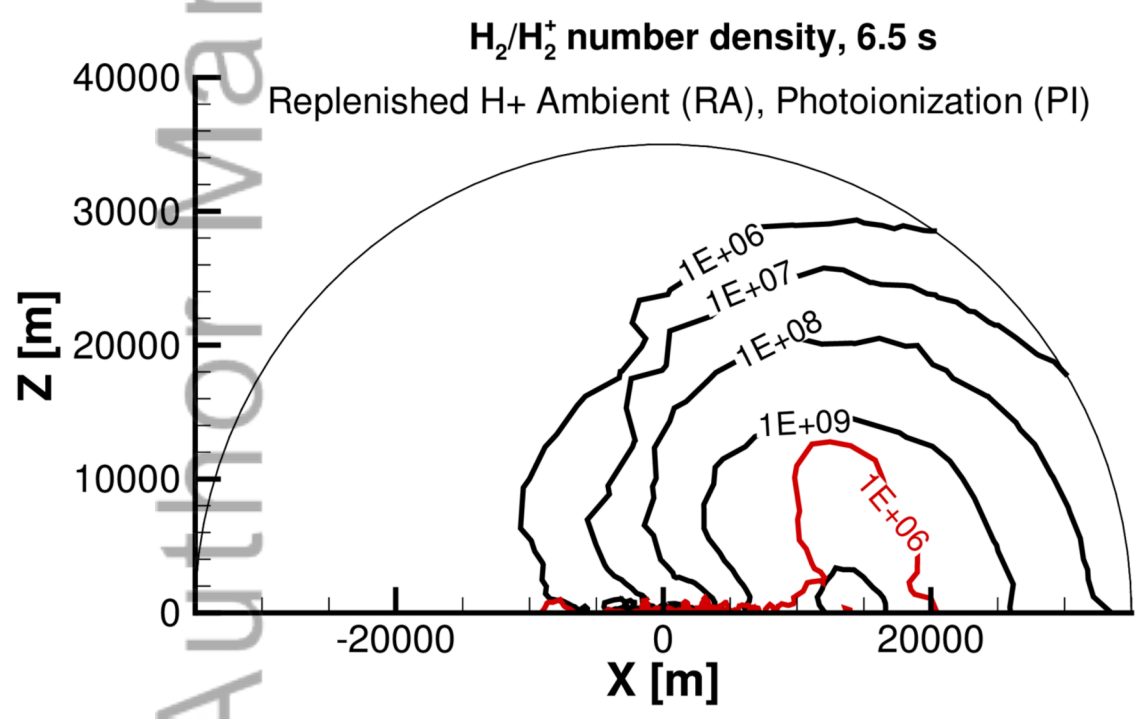


2015ja021158-f18-z-

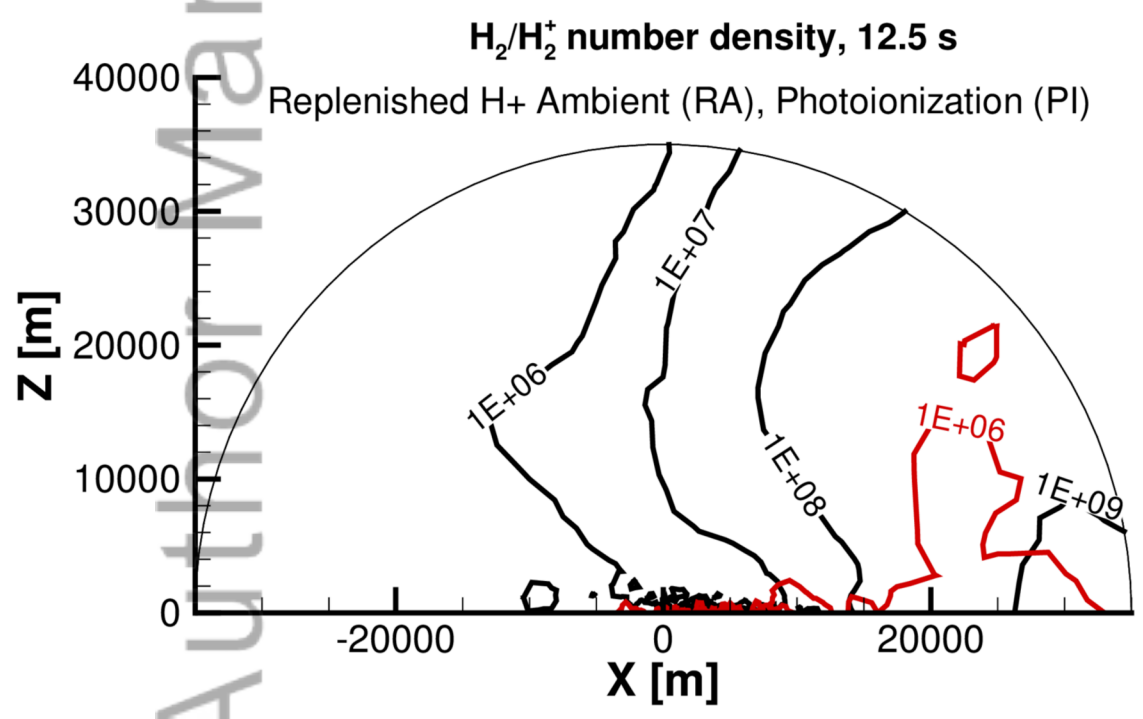




2015ja021158-f19-z-

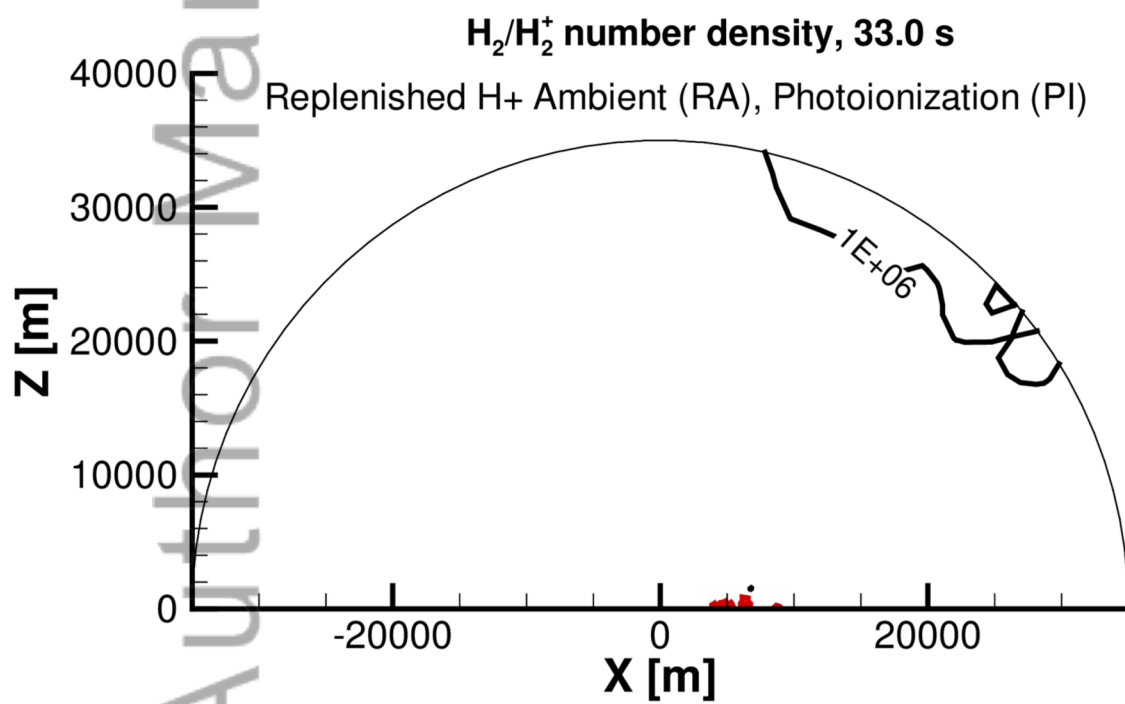


2015ja021158-f20-z-

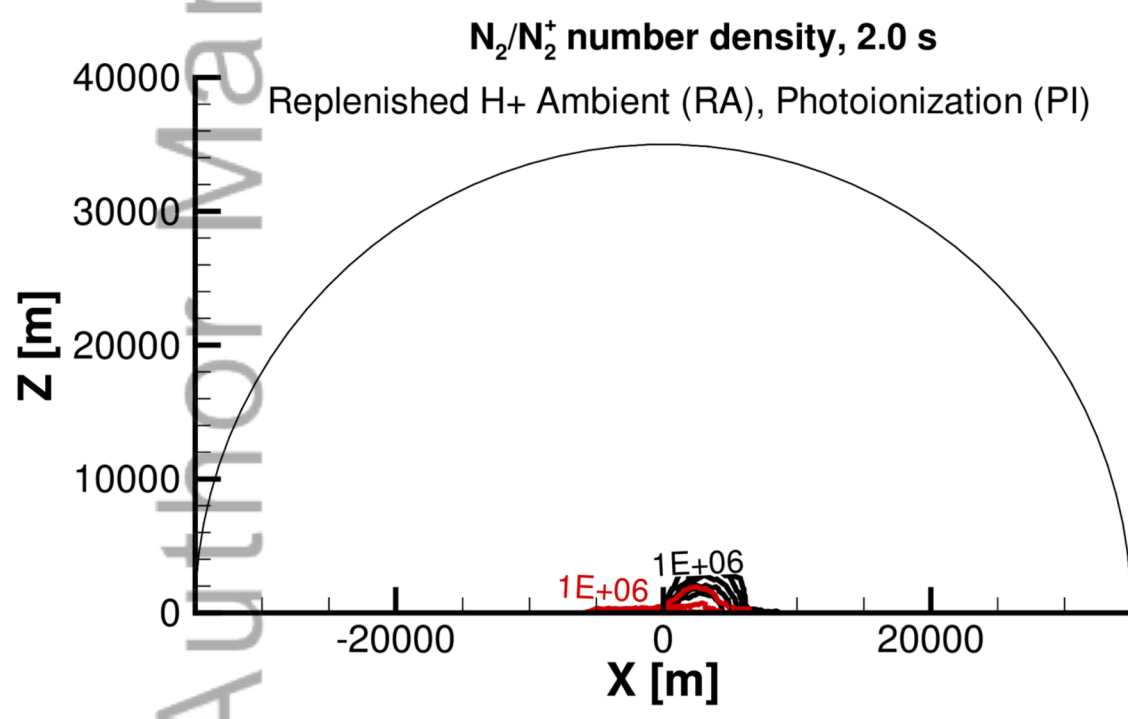


2015ja021158-f21-z-

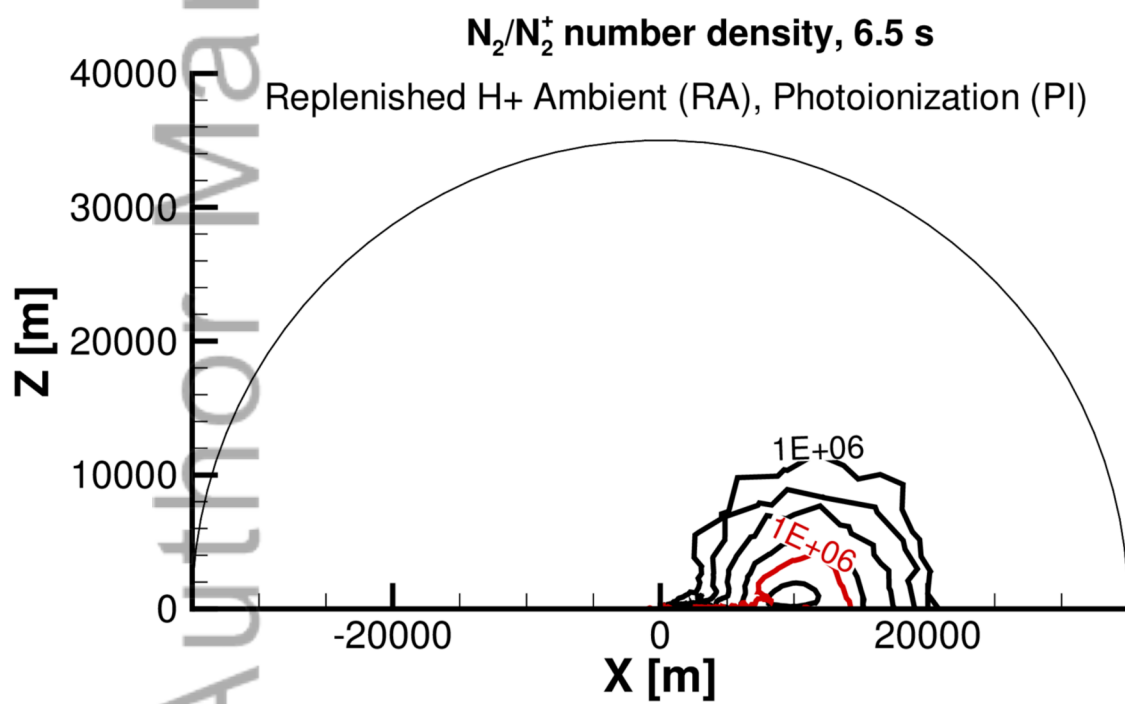
Author Manuscript



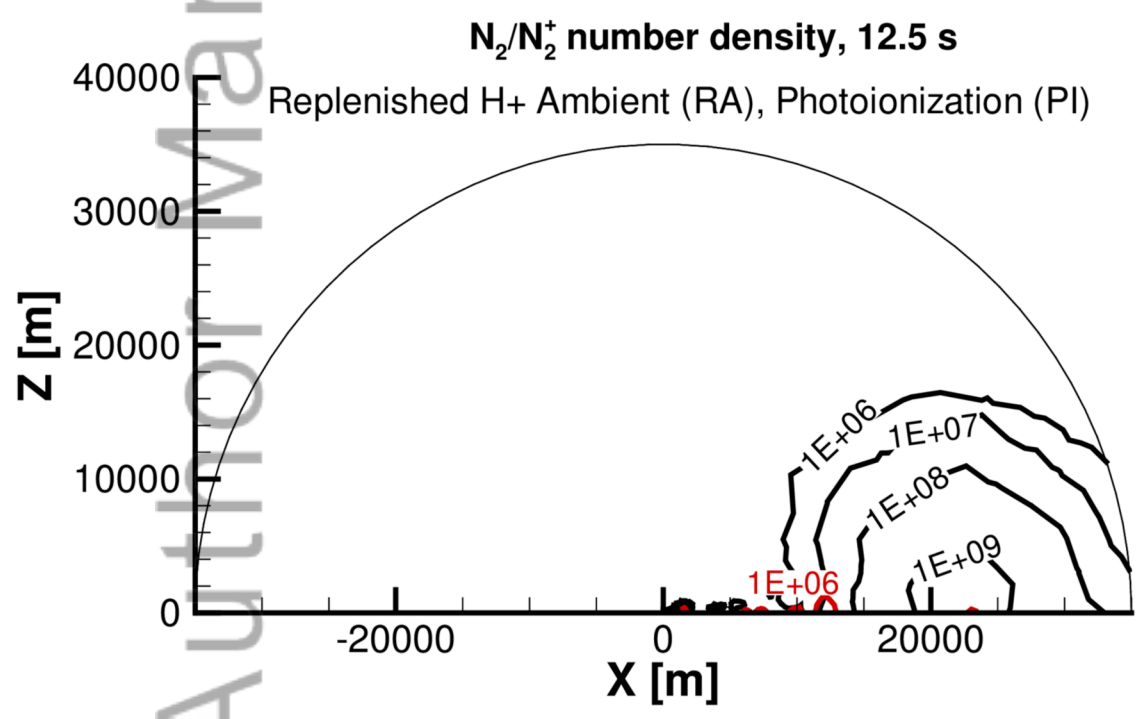
2015ja021158-f22-z-



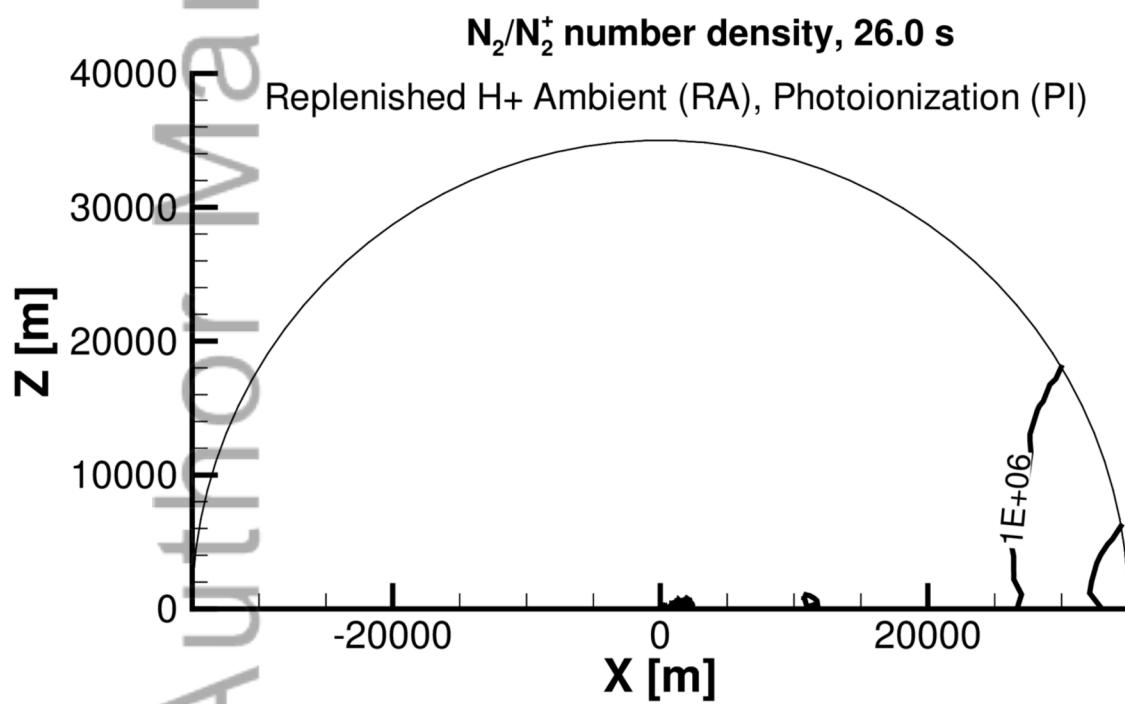
2015ja021158-f23-z-



2015ja021158-f24-z-

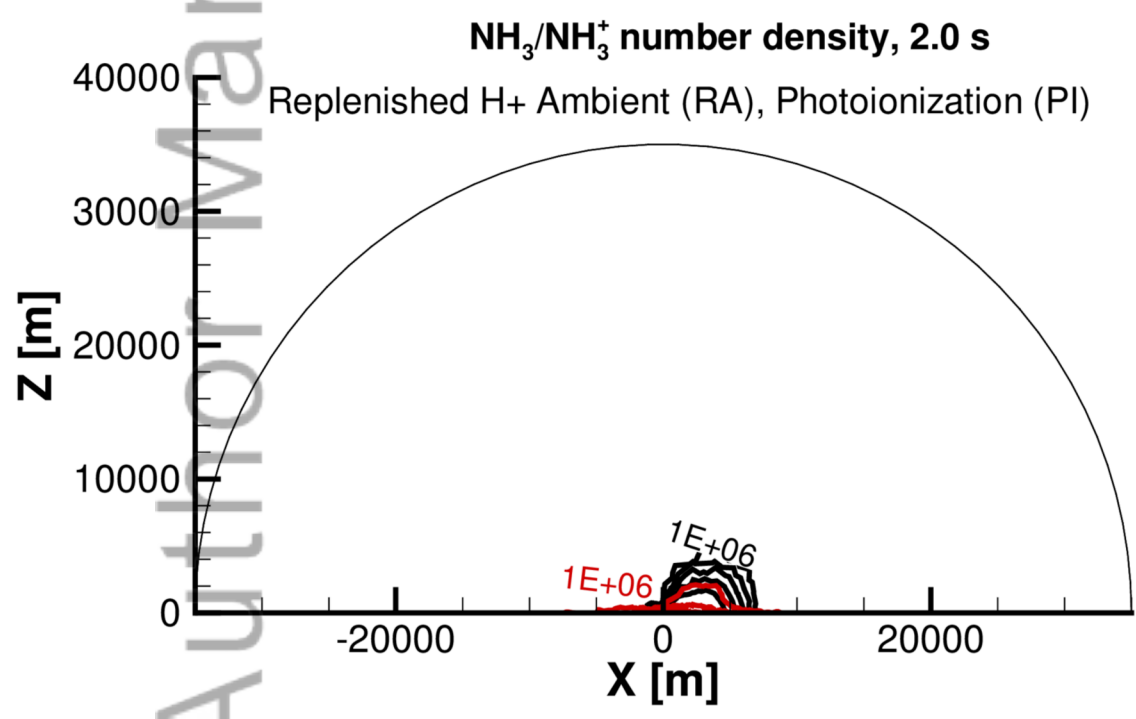


2015ja021158-f25-z-

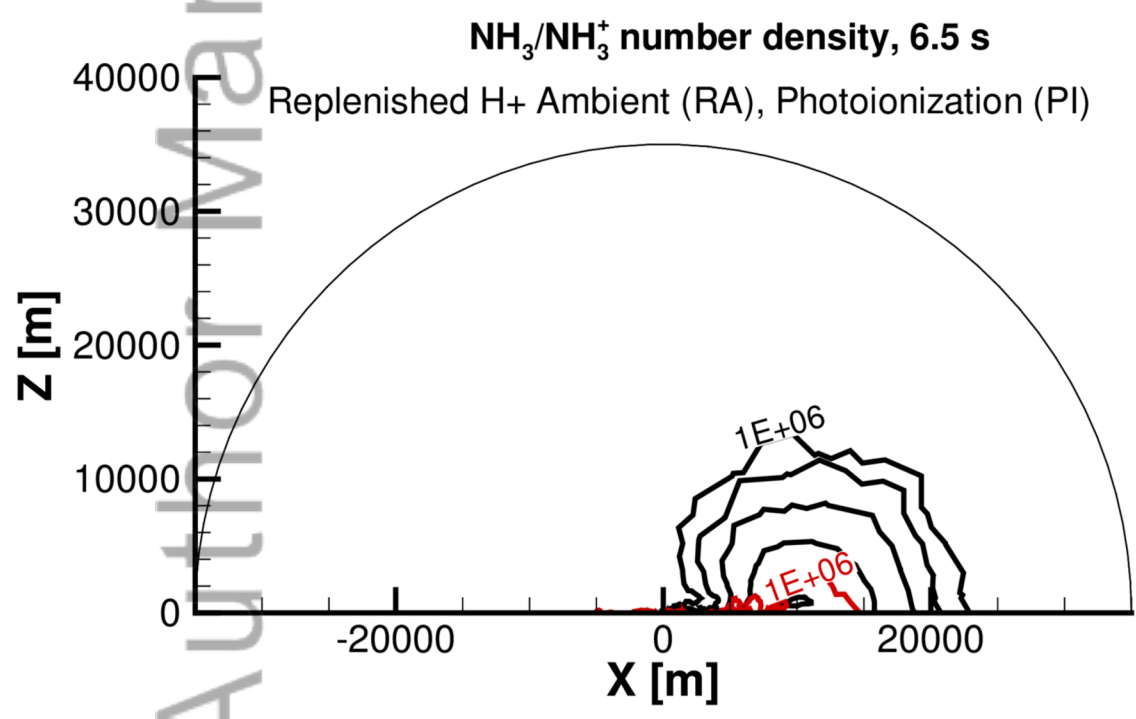


2015ja021158-f26-z-

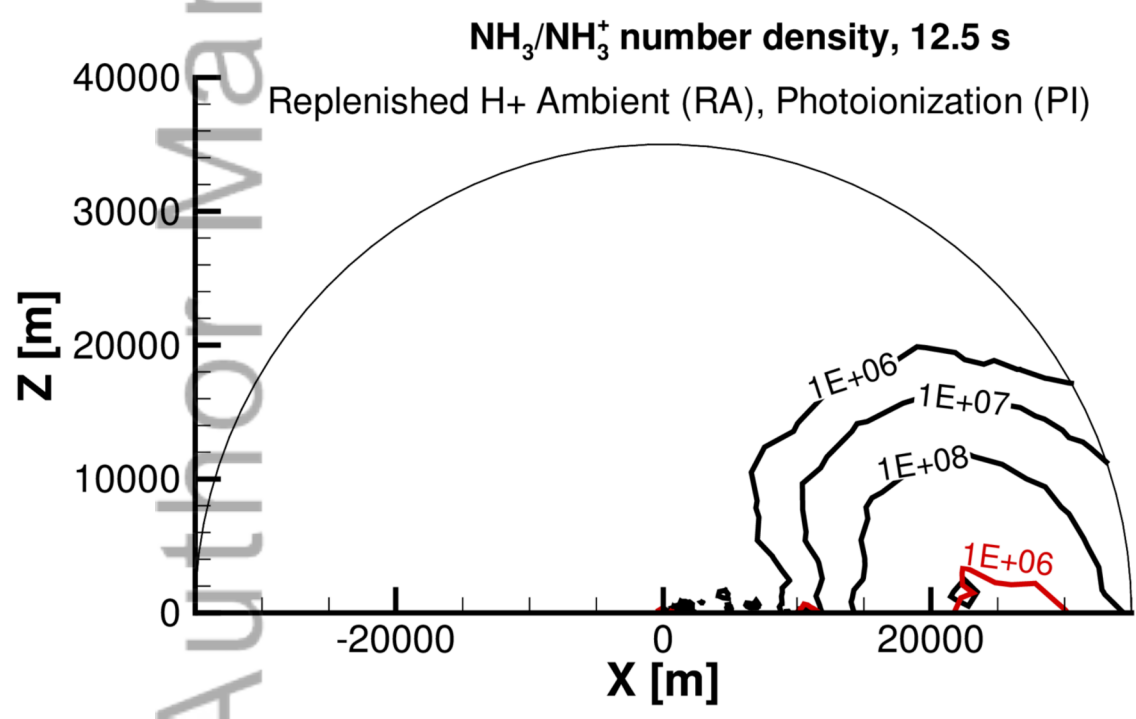




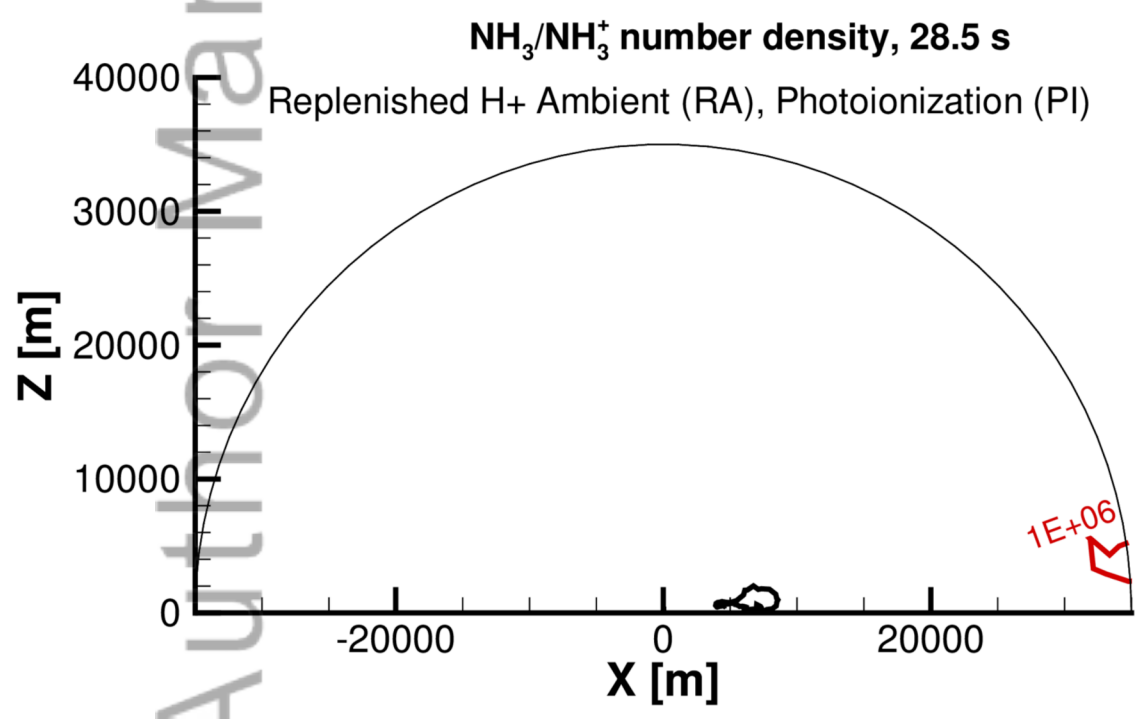
2015ja021158-f27-z-



2015ja021158-f28-z-



2015ja021158-f29-z-



2015ja021158-f30-z-